Convection-Permitting Simulations of Precipitation over the Peruvian Central Andes: Strong Sensitivity to Planetary Boundary Layer Parameterization

Yongjie Huang,[a] Ming Xue,[a,b] Xiao-Ming Hu,[a,b] Elinor Martin,[b,c] Hector Mayol Novoa,[d] Renee A. McPherson,[e,f] Andres Perez,[d] Isaac Yanqui Morales[d]

[a] *Center for Analysis and Prediction of Storms, University of Oklahoma, Norman, OK, USA*

[b] *School of Meteorology, University of Oklahoma, Norman, OK, USA*

[c] *South Central Climate Adaptation Science Center, University of Oklahoma, Norman, OK, USA*

[d] *Universidad Nacional de San Agustín de Arequipa, Arequipa, Perú*

[e] *South Central Climate Adaptation Science Center, University of Oklahoma, Norman, OK, USA*

[f] *Department of Geography and Environmental Sustainability, University of Oklahoma, Norman, OK, USA*

Corresponding author: Ming Xue, mxue@ou.edu

ABSTRACT: Regional climate dynamic downscaling at convection-permitting resolutions is now practical and has potential to significantly improve over coarser-resolution simulations, but the former is not necessarily free of systematic biases. Evaluation and optimization of model configurations are therefore important. Twelve simulations at a convection-permitting grid spacing of 3 km using the WRF model with different microphysics, planetary boundary layer (PBL), and land surface model (LSM) schemes are performed over the Peruvian Central Andes during austral summer, a region with particularly complex terrain. The simulated precipitation is evaluated using rain gauge data in Peru and three gridded precipitation datasets. All simulations correctly capture four precipitation hotspots associated with prevailing winds and terrain features along the east slope of Peruvian Central Andes, though they generally overestimate the precipitation intensity. The simulation using Thompson microphysics, ACM2 PBL and Noah LSM schemes has the smallest bias. The simulated precipitation is most sensitive to PBL schemes, secondly sensitive to microphysics and least sensitive to LSM. The simulated precipitation is generally stronger in simulations using YSU than MYNN and ACM2 PBL schemes. All simulations successfully capture the diurnal precipitation peak time mainly in the afternoon over the Peruvian Central Andes and in the early morning along its east slope. However, there are significant differences over the western Amazon Basin, where the precipitation peak occurs primarily in the late afternoon. Simulations using YSU exhibit a 4–8-hour delay in the precipitation peak over the western Amazon Basin, consistent with their stronger and more persistent low-level jets. These results provide guidance on the optimal configuration of dynamic downscaling of future global climate projections for the Peruvian Central Andes region.

1. Introduction

Due to constraints of computing resources, state-of-the-art global climate models (GCMs) are still run at coarse grid spacings (50–100 km at most, Juckes et al. 2020). Such resolutions are too coarse to resolve local-scale forcing and weather. The parameterized precipitation simulation in GCMs is generally poor (Giorgi 2019). Regional climate model (RCM) simulations nested with GCMs or regional climate dynamical downscaling have become an important tool to bring GCM resolutions to higher spatiotemporal resolutions and provide much more details on local flows and climate (e.g., Giorgi and Bates 1989; Leung et al. 2003; Giorgi 2006; Solman 2013; Rummukainen et al. 2015; Sun et al. 2016; Hu et al. 2018; Ambrizzi et al. 2019; Giorgi 2019; Kendon et al. 2021). Higher-resolution RCMs improve the representation of lower boundary forcing, including those of complex topography, land use and land cover, coastlines, as well as mesoscale dynamical processes. Therefore, high-resolution RCMs are even more important for climate studies over regions with particularly complex terrain, such as regions over the Andes in South America.

Many previous studies have indicated the added value of higher-resolution RCMs over different climate zones, compared to GCMs, lower-resolution RCMs or even low-resolution reanalyses (e.g., Feser et al. 2011; Solman 2013; Torma et al. 2015; Rummukainen 2016; Giorgi 2019; Ciarlo et al. 2020). For example, Kanamitsu and Kanamaru (2007) showed the advantage of 10-km simulation in near-surface wind and temperature over California from diurnal cycle to multidecadal trend compared to the NCEP–NCAR reanalysis at a grid spacing of ~200 km. Gao et al. (2006) demonstrated improvement in simulation of East Asian precipitation when decreasing horizontal grid spacing from 360 to 45 km. Torma et al. (2015) found substantial added value of RCMs at horizontal resolutions of 0.44° (~50 km) and 0.11° (~12 km) for different metrics of precipitation over the European Alps areas characterized by complex terrain compared to the driving GCMs. Moufouma-Okia and Jones (2015) showed improvements with increasing horizontal resolutions with grid spacings from 150 to 12 km in rainfall simulation over Africa. Lucas-Picher et al. (2017) highlighted the added value of finer resolutions in the simulations of five North American weather phenomena, including orographic precipitation and snow in the Rocky Mountains, North American monsoon, snowbelts around the Great Lakes, wind in the St. Lawrence River Valley, and diurnal cycle of precipitation over Florida and the Caribbean. Falco et al. (2020) confirmed the added value of RCMs in simulating extreme precipitation and mean surface temperature in South

America by six RCM simulations at a resolution of ~50 km from the World Climate Research Program (WCRP) Coordinated Regional Downscaling Experiment (CORDEX, Gutowski Jr et al. 2016).

All aforementioned studies ran RCMs at grid spacings of tens of kilometers, in which deep convection cannot be resolved explicitly and has to be parameterized. The parameterization of convection is considered a major source of uncertainty and has significant biases in RCM simulations of precipitation (Prein et al. 2015, 2020; Giorgi 2019; Lucas-Picher et al. 2021). In convection-permitting models (CPMs) with horizontal grid spacings of a few kilometers (generally < 4 km), convection parameterization can be switched off and deep convection can develop explicitly. Many studies have shown substantial improvements in precipitation simulation of CPMs compared to convection-parameterized models in different regions around the world, including Europe (e.g., Prein et al. 2013; Fosser et al. 2015; Berthou et al. 2020; Fumière et al. 2020; Lind et al. 2020), North America (e.g., Sun et al. 2016; Gao et al. 2017), Asia (e.g., Karki et al. 2017; Zhu et al. 2018; Li et al. 2021), Africa (e.g., Kouadio et al. 2020). Fosser et al. (2015) showed the performance of hourly intensity distribution and diurnal cycle of precipitation in southwestern Germany is significantly improved in the 2.8-km RCM simulations compared to the 50- and 7-km RCM simulations. Sun et al. (2016) showed that the 4-km convection-permitting simulation of summer precipitation over the Great Plains in the U.S. outperforms the simulation at a 25-km grid spacing in the extreme precipitation magnitude and the precipitation diurnal cycle benefiting from the more realistic simulations of the low-level jet and related atmospheric circulations in the 4-km run. Gao et al. (2017) examined simulations of the summer precipitation over the conterminous U.S. at grid spacings of 36, 12, and 4 km, and also found the 4-km convection-permitting simulations most skillfully reproduced the spatial distributions and diurnal cycle of the observed precipitation. Zhu et al. (2018) showed that forecasts at a 4-km grid spacing over China during the summer season outperformed global model forecasts in terms of spatial distribution, intensity, and diurnal variation of precipitation. These improvements of CPMs in precipitation simulation can be attributed to better resolved land surface conditions, explicit representation of convection and more realistic representation of local- and meso-scale dynamics (Prein et al. 2013; Sun et al. 2016; Zhu et al. 2018). For these reasons, convection-permitting RCM simulations have been increasingly more used whenever computational resources allow (e.g., Prein et al. 2015; Liu et al. 2017; Stratton et al.

2018; Kendon et al. 2019; Chan et al. 2020; Coppola et al. 2020; Fosser et al. 2020; Guo et al. 2020; Lind et al. 2020; Prein et al. 2020).

Weather and climate in South America are strongly influenced by the complex Andes topography and synoptic features such as the South American low-level jet (SALLJ) (Marengo et al. 2002; Vernekar et al. 2003; Vera et al. 2006; Salio et al. 2007; Romatschke and Houze Jr 2010; Mohr et al. 2014; Rasmussen and Houze Jr 2016; Jones 2019; Montini et al. 2019; Chavez et al. 2020; Poveda et al. 2020). The rising and withdrawing of nocturnal SALLJ with high instability and abundant moisture trigger the extreme austral summer convection on the east slope and foothills of the central Andes, respectively (Romatschke and Houze Jr 2010; Chavez et al. 2020). To date, there have been numerous RCM simulations conducted in South America (e.g., Roads et al. 2003; Vernekar et al. 2003; Marengo et al. 2010; Solman 2013; Gutowski Jr et al. 2016; Ambrizzi et al. 2019; Martinez et al. 2019; Solman and Blázquez 2019; Zaninelli et al. 2019; Avila-Diaz et al. 2020; Falco et al. 2020; Chimborazo and Vuille 2021; Hodnebrog et al. 2021; Martinez et al. 2022; da Silva et al. 2023). However, almost all these RCM simulations were performed at the grid spacing of tens of kilometers, and few convection-permitting RCM simulations have been conducted over South America (e.g., Schumacher et al. 2020; Bettolli et al. 2021; Lavin-Gullon et al. 2021; Junquas et al. 2022). Bettolli et al. (2021) examined four convection-permitting RCM simulations and four statistical downscaling models in simulating daily extreme precipitation events in southeastern South America in the warm season from October 2009 to March 2010, and found that most models are able to capture the selected extreme events, despite a large spread in accumulated values and the location of heavy precipitation among the models, which was also indicated by Lavin-Gullon et al. (2021). Hodnebrog et al. (2021) downscaled three GCMs to 50-km horizontal grid spacing over South America, and to 10-km grid spacing for central Chile, Peru, and southern Brazil, and found that increasing the model resolution could produce a different sign for precipitation trend projections for Peru and southern Brazil. They suggested that an ensemble of CPM simulations is necessary to increase the reliability of precipitation projection for Peru and southern Brazil, where convective precipitation is dominant. Schumacher et al. (2020) found that 3-km simulation achieves a better performance of precipitation as elevation increases, most likely due to the better-resolved topography in the Central Andes of Chile and Argentina. Some short-period modeling studies (e.g., Mourre et al. 2016; Moya-Álvarez et al. 2019; Paccini and Stevens 2023) also emphasized

the added value of convection-permitting resolutions in improving precipitation simulations across various regions in Peru and over the Amazon Basin. Supported by funding from Universidad Nacional de San Agustín de Arequipa, Arequipa, Peru, this project seeks to perform future climate projections for Peru and the surrounding regions at a 3-km grid spacing based on the Weather Research and Forecasting (WRF) model (Skamarock et al. 2019) to examine projected changes in high-impact weather events in the Peruvian Central Andes region (Poveda et al. 2020). Before actually conducting future climate simulations over decade-long periods, we want to evaluate and optimize the configurations of the model for the region.

Convection-permitting simulations of precipitation are strongly influenced by physics parameterizations, including microphysics (MP), planetary boundary layer (PBL), and land surface model (LSM) schemes (e.g., Zhu and Xue 2016; Feng et al. 2018; Guo et al. 2019; He et al. 2019; Huang et al. 2020; Kouadio et al. 2020; Taraphdar et al. 2021; González-Rojí et al. 2022). González-Rojí et al. (2022) examined the sensitivity of precipitation over southern Peru to physics parameterization schemes in WRF V3.8.1, however, very limited physics schemes and combinations were tested in their study. As the first step to conduct long-term convection-permitting regional climate simulation, a series of two-month convection-permitting simulations using different physics parameterization schemes are performed over the Peruvian Central Andes during austral summer using the planned nested grid configuration. It should be noted that initially a configuration using Thompson MP, YSU PBL, and Noah LSM schemes based on previous studies was used to make a 10-year simulation over 2010–2019. It was found that precipitation was significantly over-predicted (Chen et al. 2022), which also motivated this study to compare configurations using combinations of different MP, PBL, and LSM schemes. The main objective of this study is to evaluate the performance of WRF-based CPMs in simulating precipitation over the Peruvian Central Andes by comparing with available best observational data. The results of this study will provide guidance on the optimal configuration of CPM for future climate dynamic downscaling for the Peruvian Central Andes region.

The rest of this paper is organized as follows. Section 2 describes the model and experiment setup and observational data used for evaluation. Section 3 presents and discusses the precipitation evaluation results. A summary is presented in Section 4.

2. Method and data

a. Model setup

The WRF model Version 4.2.1 (Skamarock et al. 2019) is used. The hourly European Centre for Medium-Range Weather Forecasts Reanalysis v5 (ERA5) data (Hersbach et al. 2020) are used for initial and boundary conditions for the simulations. Two one-way nested domains at 15- and 3-km horizontal grid spacings are used, which cover the entire South America and the Peruvian central Andes region, respectively (Fig. 1a). Both domains use 61 stretched vertical levels topped at 20 hPa. Spectral nudging technique (Miguez-Macho et al. 2004) is applied to the outer 15-km domain to maintain large-scale circulations. The spectral nudging configurations are similar to those in Hu et al. (2018). The nudging variables include horizontal wind components, temperature, moisture, and geopotential height above PBL height. Nudging wave numbers of 5 and 3 in the zonal and meridional directions and nudging coefficient of 3×10^{-5} s^{-1} are adopted throughout the simulation period. The simulations cover two months (January and February 2019) during the austral summer with the first month treated as the spin-up period mainly for land surface models. Limited by computational resources, the simulations cannot span over multiple years. Based on the assumption that the relative performance for precipitation can be revealed by simulations over a couple of months in the rainy season, we choose to run over two months from January to February, which are the climatological peak months of precipitation during the austral summer (Mohr et al. 2014; Espinoza et al. 2015).

The combinations of MP, PBL and LSM schemes of the 12 sensitivity experiments examined in this study are listed in Table 1. The MP schemes include the Thompson scheme (THOM) (Thompson et al. 2008), Thompson aerosol-aware scheme (THOMA) (Thompson and Eidhammer 2014), WRF Single–moment 6–class scheme (WSM6) (Hong and Lim 2006), and Morrison 2–moment scheme (MORR) (Morrison et al. 2009). The PBL schemes include Yonsei University scheme (YSU) (Hong and Lim 2006), Mellor–Yamada Nakanishi Niino (MYNN) level 2.5 scheme (Nakanishi and Niino 2009), and Asymmetric Convection Model 2 scheme (ACM2) (Pleim 2007). The LSM schemes include the unified Noah LSM (Noah) (Ek et al. 2003), Noah multiple-physics LSM (NoahMP) (Niu et al. 2011), and Community Land Model (CLM) version 4 (Lawrence et al. 2011). Other physics parameterizations are the same among the sensitivity experiments, including

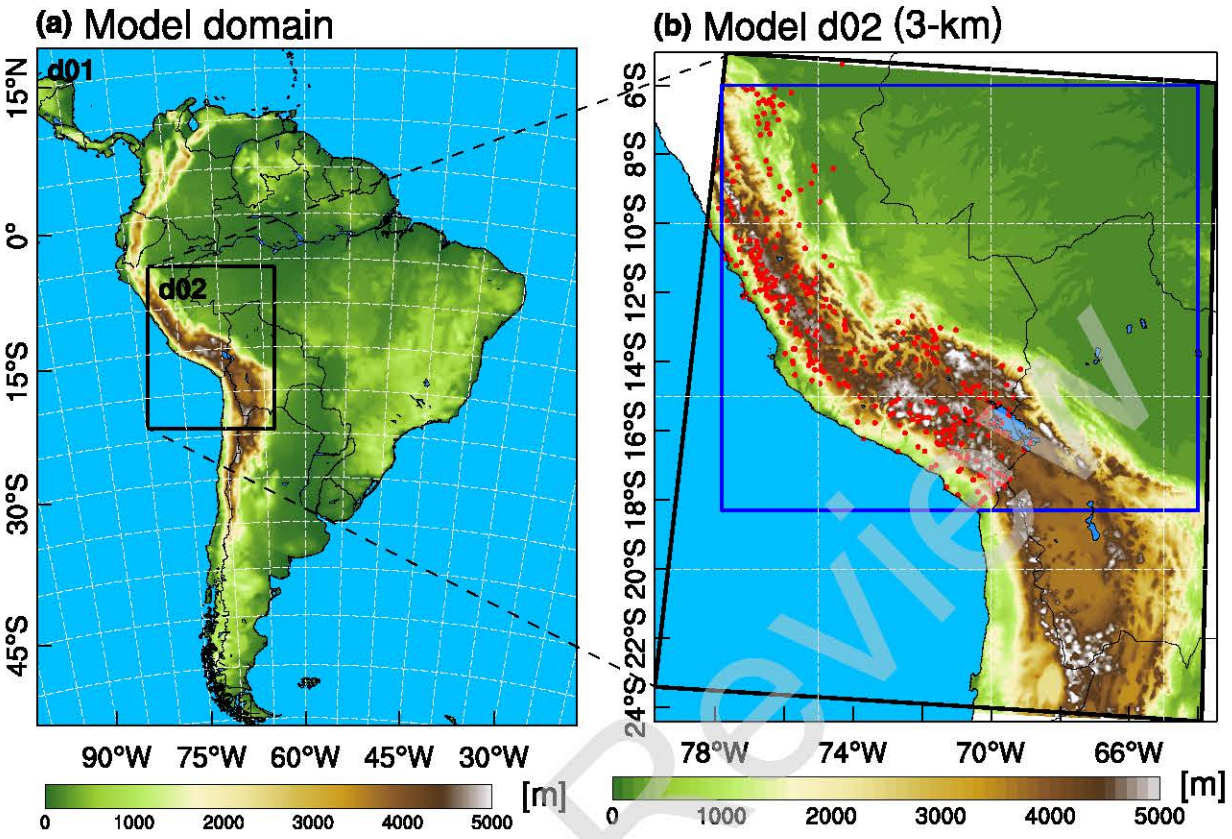

FIG. 1. (a) The model domain configuration (color shaded fields represent terrain elevation, in m). (b) Terrain elevation in the 3-km domain with rain gauge locations marked by red dots. The blue rectangle indicates the study area in this study.

the revised MM5 Monin-Obukhov surface layer scheme (Jiménez et al. 2012), and the RRTMG (the Rapid Radiative Transfer Model) longwave and shortwave radiation schemes (Iacono et al. 2008). The Tiedtke cumulus parameterization scheme (Tiedtke 1989) is used only for the 15-km domain.

b. Observational data

Three gridded global precipitation datasets including half-hourly Integrated Multi-satellitE Retrievals for GPM (IMERG) at a horizontal resolution of 0.1° × 0.1° (Huffman et al. 2019), half-hourly NOAA Climate Prediction Center (CPC) MORPHing Technique (CMORPH) global precipitation analyses at a horizontal grid spacing of ~8 km (Joyce et al. 2004), and 3-hourly Multi-Source Weighted-Ensemble Precipitation (MSWEP) version 2 at a horizontal resolution of 0.1° × 0.1°

TABLE 1. Physics parameterization schemes in the 12 sensitivity experiments

Experiment	MP	PBL	LSM
THOM_YSU_Noah	THOM	YSU	Noah
THOM_YSU_NoahMP	THOM	YSU	NoahMP
THOM_YSU_CLM	THOM	YSU	CLM
THOM_MYNN_Noah	THOM	MYNN	Noah
THOM_MYNN_NoahMP	THOM	MYNN	NoahMP
THOM_ACM2_Noah	THOM	ACM2	Noah
THOM_ACM2_NoahMP	THOM	ACM2	NoahMP
THOMA_YSU_Noah	THOMA	YSU	Noah
WSM6_YSU_Noah	WSM6	YSU	Noah
WSM6_MYNN_Noah	WSM6	MYNN	Noah
MORR_YSU_Noah	MORR	YSU	Noah
MORR_MYNN_Noah	MORR	MYNN	Noah

(Beck et al. 2019) are used for the evaluation of simulated monthly and diurnal precipitation. IMERG incorporates monthly gauge analysis product produced by the Global Precipitation Climatology Centre (GPCC) at the grid spacing of 1° (Huffman et al. 2019), and MSWEP uses daily observations from gauges worldwide to determine the merging weights, calculate the wet-day biases for the reanalyses, and correct the precipitation estimates near gauge stations (Beck et al. 2019). However, gauge stations used by IMERG and MSWEP are very sparse in our study region (Huffman et al. 2019; Beck et al. 2019). CMOPRH does not blend rainfall station gauge data into its estimates (Joyce et al. 2004). Monthly precipitation data of about 400 rain gauge stations in Peru (Fig. 1b, Aybar et al. 2020) are also used for the evaluation of global precipitation datasets and simulated precipitation. Due to the limited spatial coverage and coarse temporal resolutions of rain gauge data, evaluations of spatial distribution and diurnal cycle of precipitation are mainly based on the global precipitation datasets.

For the comparison among the precipitation datasets at different resolutions, CMORPH, MSWEP and the simulated precipitation fields are regridded to the IMERG grid ($0.1° \times 0.1°$) by using the "patch recovery" technique (Sun et al. 2016).

c. Evaluation metrics

The mean bias (MB) is used to examine the mean error, given by

$$\mathrm{MB} = \frac{1}{N}\sum_{i=1}^{N}(M_i - O_i), \tag{1}$$

where N is the total number of samples, M and O represent simulations and observations, respectively.

The root mean square error (RMSE) is selected to examine the average magnitude of the simulation errors, which is

$$\mathrm{RMSE} = \sqrt{\frac{1}{N}\sum_{i=1}^{N}(M_i - O_i)^2}. \tag{2}$$

To characterize the variation/shape of the distribution for a given variable, Taylor Skill Score (TSS) (Taylor 2001) is adopted and given by,

$$\mathrm{TSS} = \frac{4(1+R)}{\left[\left(\sigma_r + \frac{1}{\sigma_r}\right)^2 (1+R_0)\right]}, \tag{3}$$

where σ_r is the normalized standard deviation given by simulated root mean square (RMS) divided by the observed RMS, R is the correlation coefficient, and R_0 is the maximum correlation attainable, which is set to 1. Thus, if the correlation coefficient and normalized standard deviation are 1, TSS is 1.

3. Results

a. Monthly precipitation

Mean daily precipitation of the three precipitation products and simulations in February 2019 are shown in Fig. 2 to examine the spatial distribution characteristics. Similar results were found in January 2019 although it is treated as the spin-up period. Thus, results in February 2019 are discussed in detail here. There are four precipitation hotspots along the east slope of the Peruvian Central Andes (marked by numbers in white in Fig. 2), although there exists a difference in precipitation intensity among the three precipitation products (Figs. 2a–c). The four hotspots are

all near the notches of terrain, indicating that terrain plays an important role in producing these hotspots, which was also indicated in previous studies (e.g., Mohr et al. 2014; Espinoza et al. 2015; Chavez and Takahashi 2017; Junquas et al. 2018). Precipitation from IMERG and MSWEP are closer to each other in terms of precipitation distribution and intensity over the western Amazon Basin to the east of the Peruvian Central Andes (Figs. 2a and c). All simulations successfully capture the four precipitation hotspots. However, they overestimate their intensity compared to IMERG and MSWEP, with the maximum precipitation intensity being generally over 16 mm day^{-1} (Fig. 2). The mean daily precipitation over the entire western Amazon Basin is larger than 16 mm day^{-1} in the simulations using YSU PBL scheme combined with different MP and LSM schemes (Figs. 2d, e, f, k, l, and n), while both those in IMERG and MSWEP are less than 16 mm day^{-1} in this region (Figs. 2a and c). It means that no matter what MP or LSM schemes are used, simulations using YSU PBL scheme tend to produce larger mean daily precipitation. The MYNN PBL scheme (Figs. 2g, h, m and o) simulates a smaller area and ACM2 PBL scheme (Figs. 2d, e, f, k, l, and n) simulates an even smaller area with precipitation over 16 mm day^{-1} in the western Amazon Basin. Therefore, among the MP, PBL, and LSM schemes tested in this study, WRF simulations of total precipitation are the most sensitive to the PBL scheme, followed by the MP scheme, and least sensitive to the LSM scheme (Figs. 2d–o). It should be noted that the findings regarding the sensitivity of WRF simulations of total precipitation are based on the schemes tested in this study, which may not cover all possible configurations.

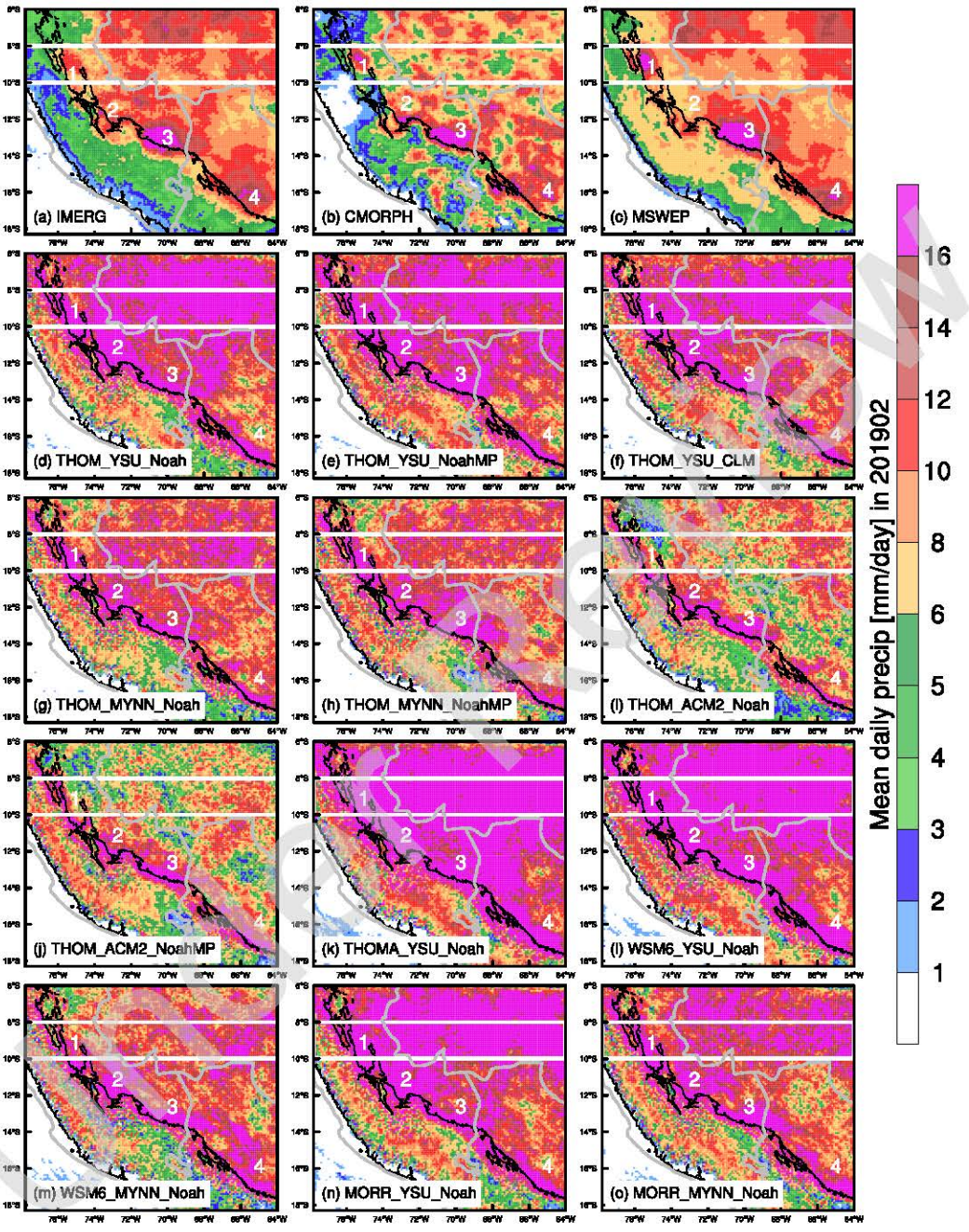

250 FIG. 2. Monthly precipitation (shaded, mm day^{-1}) of (a–c) precipitation products and (d–o) WRF simulations
251 using different physics schemes in February 2019. The black contour in each panel represents 1-km terrain
252 elevation. The white rectangle in each panel indicates the region for the Hovmöller diagram in Fig. 7.

In February 2019, compared to the rain gauge data (mean daily precipitation of ~5.25 mm day^{-1}), IMERG and CMORPH generally underestimate the mean daily precipitation with the mean biases of -1.70 and -1.90 mm day^{-1}, respectively (Figs. 3a and b), while MSWEP generally has positive bias with the mean bias of 0.29 mm day^{-1} (Fig. 3c). Among the three precipitation products (Figs. 3a–c), MSWEP has the smallest RMSE of 2.08 mm day^{-1}, while RMSEs in IMERG and CMORPH are 2.87 and 3.80 mm day^{-1} respectively. Thus, precipitation of MSWEP is closer to rain gauge data than those of IMERG and CMORPH. All simulations generally overestimate precipitation (Figs. 3d–o) with the smallest mean bias of 0.49 mm day^{-1} and RMSE of 2.85 mm day^{-1} in THOM_ACM2_Noah (Fig. 3i) and the largest mean bias of 3.92 mm day^{-1} and RMSE of 6.00 mm day^{-1} in THOMA_YSU_Noah (Fig. 3k).

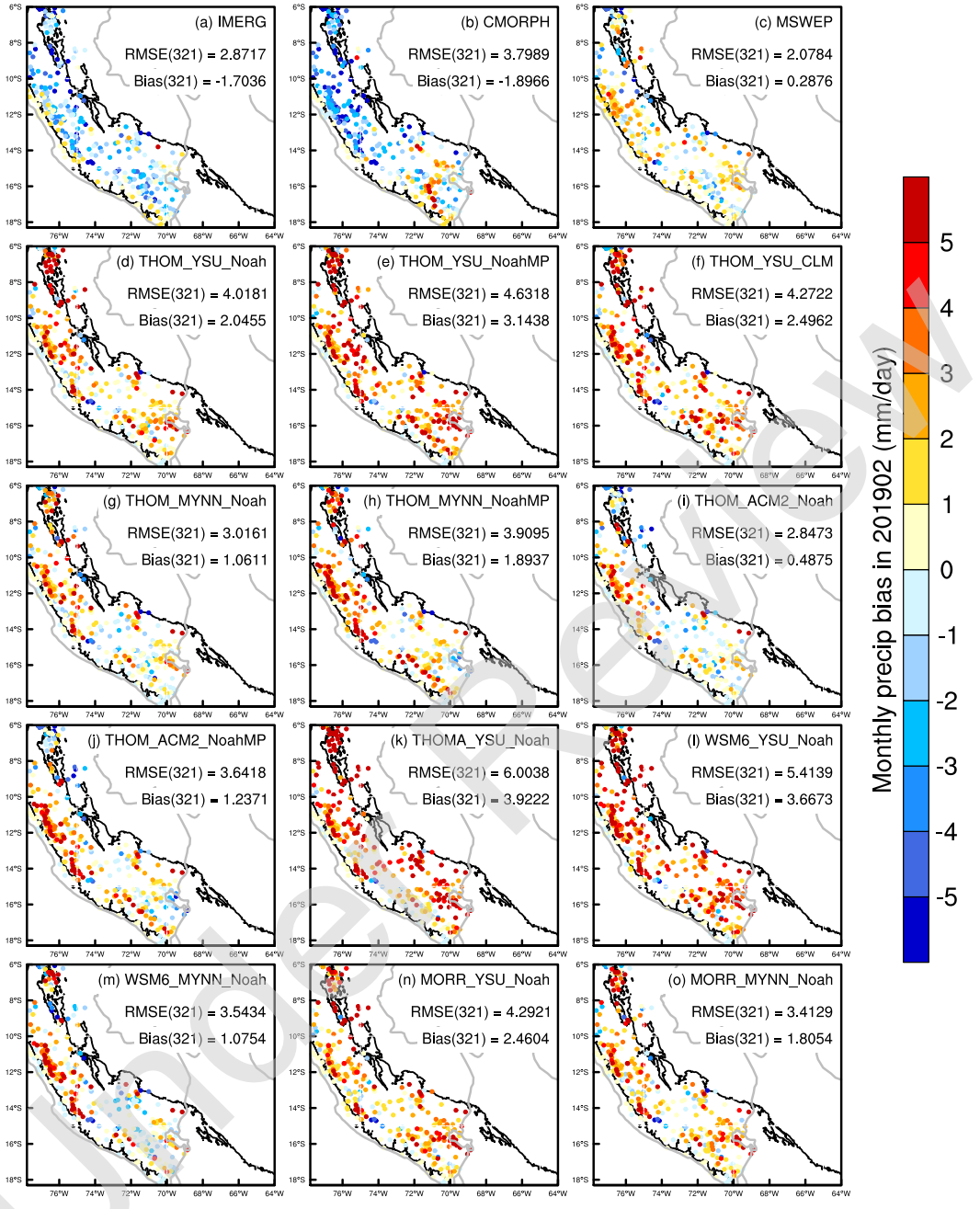

FIG. 3. Monthly precipitation biases (difference between (a–c) precipitation products or (d–o) WRF simulations in 3-km domain using different physics schemes and the rain gauge data, in mm day^{-1}) in February 2019. The root mean squared error (RMSE) and mean bias along with the number of samples in parentheses are given in each panel. The black contour in each panel represents 1-km terrain elevation.

To quantify the differences, TSS as a function of relative mean (simulated mean divided by referenced mean), and mean bias as a function of RMSE of simulated mean daily precipitation in February 2019 relative to IMERG, CMORPH, and MSWEP, respectively (Fig. 4), are examined. The results based on IMERG and MSWEP are similar to each other, while they are more different from those based on CMORPH. As discussed above, IMERG and MSWEP are more reliable than CMORPH, therefore our further discussions are mainly based on MSWEP. Among all simulations, THOM_ACM2_Noah has the highest TSS (~0.76) and its relative mean is close to 1 (Fig. 4a). Meanwhile, THOM_ACM2_Noah has the lowest RMSE (~4.4 mm day^{-1}) and its mean bias is near 0 (Fig. 4b). Therefore, based on these metrics, THOM_ACM2_Noah is generally better than the other simulations. Changing the LSM to NoahMP, the TSS, bias and RMSE in THOM_ACM2_NoahMP are changed slightly to ~0.73, ~ −0.25 mm day^{-1} and ~4.8 mm day^{-1}, respectively (Fig. 4). However, changing the PBL scheme, TSS, bias and RMSE are changed significantly to ~0.55, ~4.8 mm day^{-1} and ~8.0 mm day^{-1} respectively in THOM_YSU_Noah and to ~0.68, ~2.3 mm day^{-1} and ~5.6 mm day^{-1} respectively in THOM_MYNN_Noah (Fig. 4). When changing the MP scheme, the ranges of TSS, bias and RMSE are ~0.13 (0.42–0.55), ~3.4 (4.8–8.2) mm day^{-1} and ~3.5 (8.0–11.5) mm day^{-1} respectively among the simulations of THOM_YSU_Noah, THOMA_YSU_Noah, WSM6_YSU_Noah, and MORR_YSU_Noah. Their ranges are ~0.03 (0.67–0.70), ~1.2 (1.9–3.1) mm day^{-1} and ~0.7 (5.3–6.0) mm day^{-1} respectively among the simulations of THOM_MYNN_Noah, WSM6_MYNN_Noah, and MORR_MYNN_Noah. They are all smaller than the ranges of changing the PBL scheme, which are ~0.21 (0.55–0.76), ~4.8 (0.0–4.8) mm day^{-1} and ~3.6 (4.4–8.0) mm day^{-1} respectively among the simulations of THOM_YSU_Noah, THOM_MYNN_Noah, and THOM_ACM2_Noah. Therefore, based on these objective metrics, simulations are more sensitive to the PBL scheme among the schemes tested in this study and simulation THOM_ACM2_Noah is the closest to precipitation products IMERG and MSWEP.

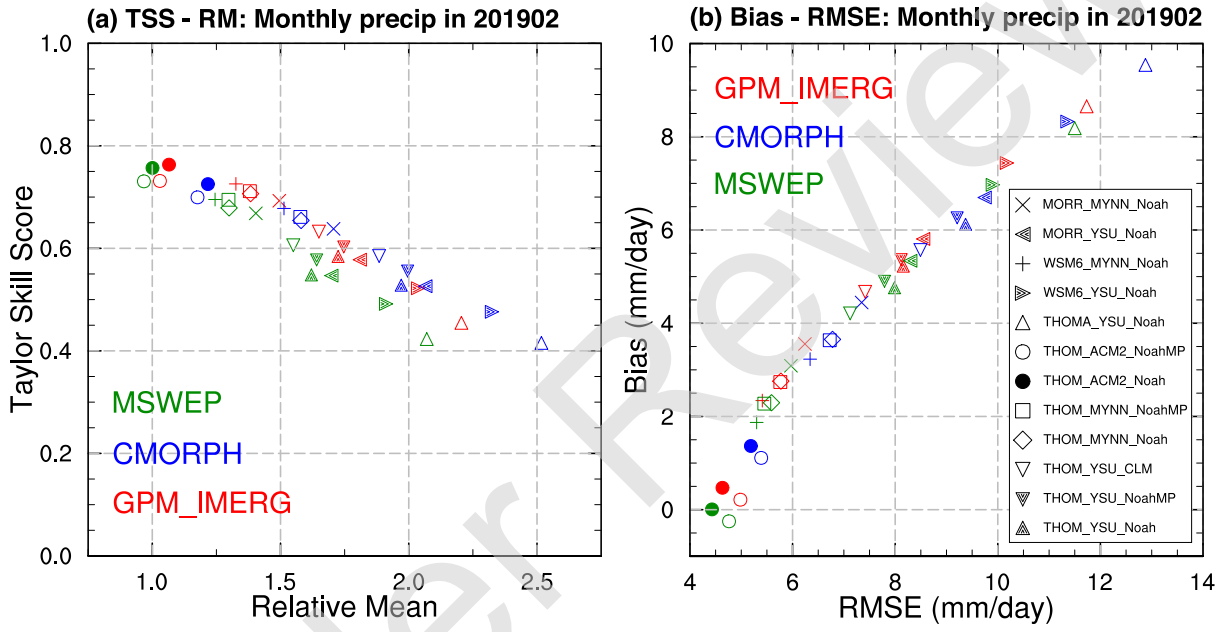

291 FIG. 4. Scatter plots of (a) Taylor Skill Score (TSS) as a function of relative mean (simulated mean divided
292 by referenced mean) and (b) bias (mm day^{-1}) as a function of root mean squared error (RMSE, mm day^{-1})
293 of simulated monthly precipitation in February 2019 relative to IMERG (red), CMORPH (blue), and MSWEP
294 (green), respectively.

b. Diurnal cycle of precipitation

Figure 5 shows the precipitation peak time calculated from hourly precipitation of IMERG, CMORPH, and simulations using different physics schemes in February 2019. The average diurnal precipitation in the mountain, foothill, and plain regions are displayed in Fig. 6. Because MSWEP is 3-hourly average precipitation and it cannot accurately depict the precipitation peak (Fig. 6), it is not included in Fig. 5. Although there are differences in precipitation intensity between IMERG and CMORPH (Figs. 2a and b), their precipitation peak times are very consistent with each other (Figs. 5a and b). Previous studies (e.g., Dezfuli et al. 2017; Sungmin and Kirstetter 2018; Tan et al. 2019; Watters and Battaglia 2019; Afonso et al. 2020) have demonstrated that IMERG has the ability to accurately capture the diurnal cycle of precipitation in different regions including South America. Over the Peruvian Central Andes for terrain elevation higher than 1 km, the precipitation peak time is mainly in the afternoon during ~14–19 LST (Figs. 5a and b). The average precipitation peak in the mountain region is at about 16 LST with ~0.47 and ~0.33 mm h^{-1} in IMERG and CMORPH respectively (Fig. 6a). Along the east slope of the Peruvian Central Andes for terrain elevations less than 1 km, the precipitation peak time is mainly in the early morning (~0–6 LST, Figs. 5a, 5b, and 6b). Over the western Amazon Basin to the east of the Peruvian Central Andes, the precipitation peak time is mainly during ~11–17 LST (Figs. 5a and b) with the maximum average precipitation of ~0.84 and ~0.80 mm h^{-1} in IMERG and CMORPH respectively (Fig. 6c). The simulations successfully capture the precipitation peak time over the Peruvian Central Andes and also along its east slope (Figs. 5c–n), with their precipitation peak times basically in the same time periods as those of IMERG and CMORPH. However, all simulations overestimate the precipitation intensity in these periods with the simulations using ACM2 PBL scheme being closer to IMERG (Figs. 6a and b). There exist larger differences in the simulated precipitation peak time over the western Amazon Basin compared to the observed (Fig. 5). In the simulations using the YSU PBL scheme (except MORR_YSU_Noah), the precipitation peak time in the region (8°–11°S, 67°–70°W) over the western Amazon Basin is delayed by about 4–8 hours compared to those of IMERG and CMORPH (Figs. 5a–e, j, k, and m), and their averaged precipitation has two peaks at ~13 and ~2 LST (Fig. 6c). The precipitation at the latter peak can be reduced when using other PBL schemes, especially the ACM2 scheme (Fig. 6c), thus the delay bias in the simulated precipitation peak time can also be reduced (Figs. 5f–i, l, and n).

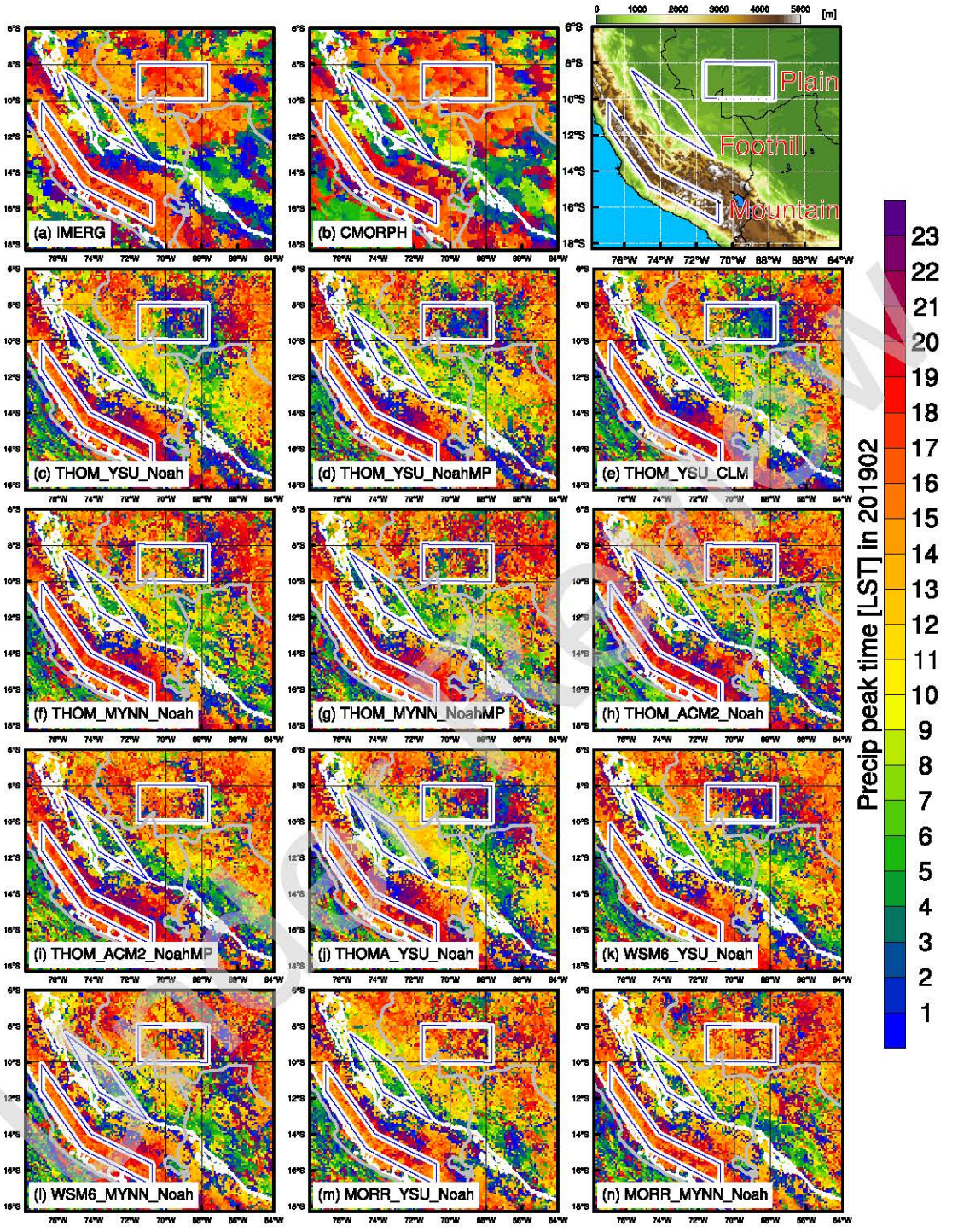

FIG. 5. Precipitation peak time (shaded, Local Standard Time, LST) calculated from (a) IMERG, (b) CMORPH, and (c–n) WRF simulations using different physics schemes in February 2019. The white contour in each panel represents 1-km terrain elevation. The blue polygons in each panel indicate the regions for diurnal precipitation calculation shown in Fig. 6 and terrain height in the study region is shown in the top-right panel. The black rectangles in each panel indicate the regions for Figs. 9 and 10.

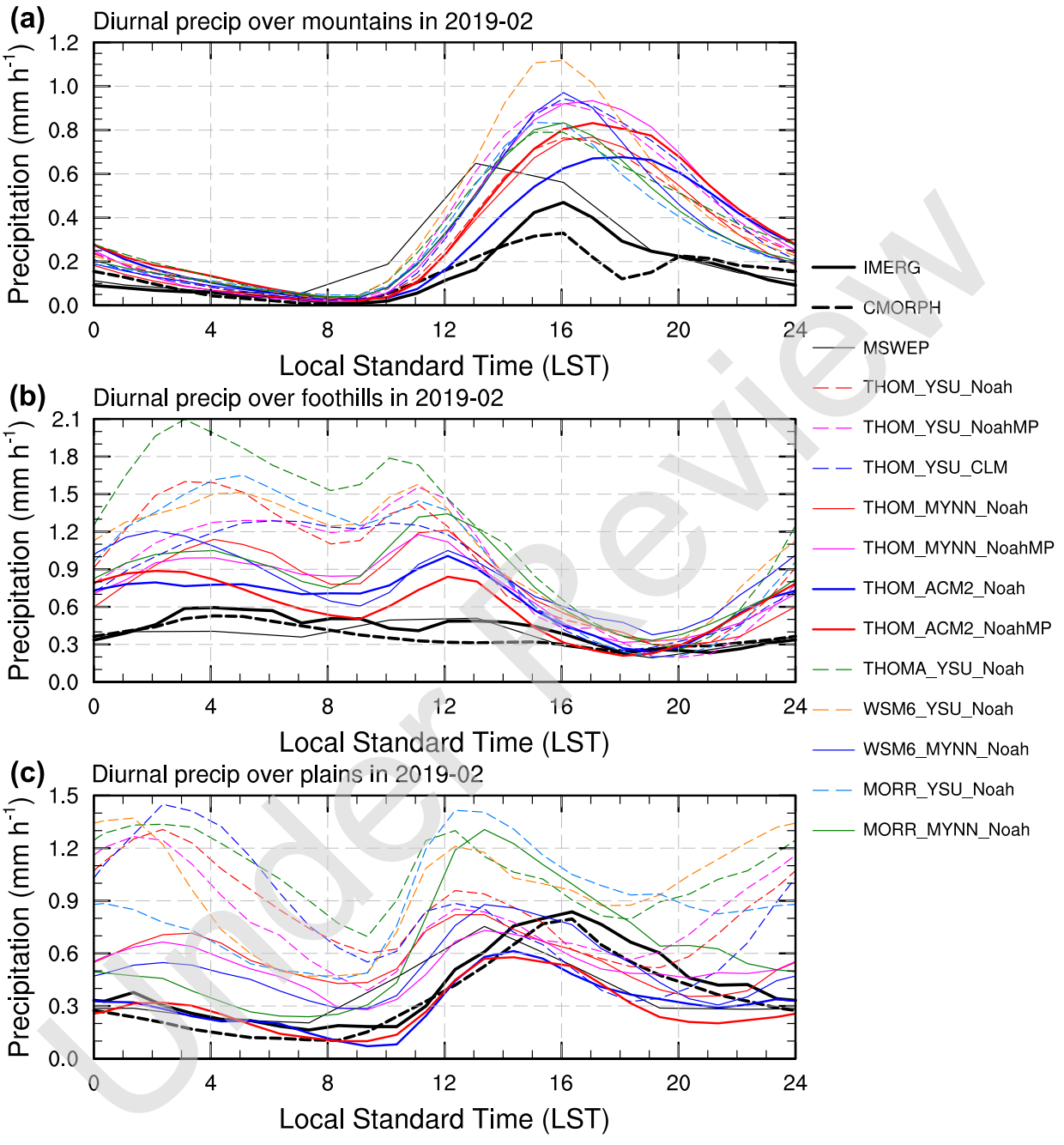

FIG. 6. Averaged diurnal precipitation (mm h^{-1}) in the (a) mountain, (b) foothill, and (c) plain regions shown in Fig. 5 from IMERG, CMORPH, MSWEP (3-hourly mean), and WRF simulations using different physics schemes in February 2019.

To examine the evolution of diurnal precipitation in the region with a larger bias over the western Amazon Basin, Hovmöller diagrams of precipitation from IMERG, CMORPH, and simulations using different physics schemes in February 2019 are created and shown in Fig. 7. The precipitation evolution between IMERG and CMORPH are very consistent with each other (Figs. 7a and b). Precipitation over the Andes for terrain elevations higher than 2 km (~78°–76°W) mainly starts at ~16 UTC (11 LST) and ends at ~8 UTC (3 LST) next day (Figs. 7a and b). At the east slope and foothills of Andes for terrain elevations lower than 2 km (~76°–74°W), precipitation has a peak between 8–12 UTC (3–7 LST) (Figs. 7a and b), which is consistent with that shown in (Figs. 5a and b). Over the western Amazon Basin (~74°–66°W), precipitation is mainly during ~15–24 UTC (10–19 LST) and can be extended to 8 UTC (3 LST) next day for the region between 72°–68°W with the peak at around 21 UTC (16 LST) (Figs. 7a and b). All simulations basically capture the main precipitation period over the Andes, at the east slope and foothills of the Andes, and over the western Amazon Basin (Figs. 7c–n), however, the simulated precipitation intensities are overestimated, especially for the simulations using the YSU PBL scheme with large areas of precipitation > 1.4 mm h^{-1}. The precipitation peak in the region between 70°–66°W is mainly within 0–12 UTC (19–7 LST) in the simulations using the YSU PBL scheme except for MORR_YSU_Noah (Figs. 7c–e, j, k, and m), which is different from those of IMERG and CMORPH (Figs. 7a and b). This bias can be reduced in simulations using other PBL schemes especially the ACM2 scheme (Figs. 7f–i, l, and n). Generally, the precipitation evolution and intensity in THOM_ACM2_Noah are closer to IMERG than in other simulations. These results are consistent with those shown in Figs. 2 and 5.

Overall, through the subjective and objective evaluation of monthly and diurnal precipitation, all simulations generally capture the main characteristics of observations, while they generally overestimate precipitation amount, especially in complex terrain regions, which is similar to previous CPM studies in different regions, such as East Asia (Guo et al. 2019; Gao et al. 2020; Li et al. 2020; Yun et al. 2020), European region (Kendon et al. 2012; Ban et al. 2014; Adinolfi et al. 2020), West Africa (Berthou et al. 2019), and Andes region (Mourre et al. 2016; Moya-Álvarez et al. 2019; Junquas et al. 2022). However, in the United States, there is a general dry bias over the central and southeast plains and a positive precipitation bias over the Rockies during the boreal warm season (Sun et al. 2016; Liu et al. 2017; Gensini et al. 2022). In the meanwhile, the simulation

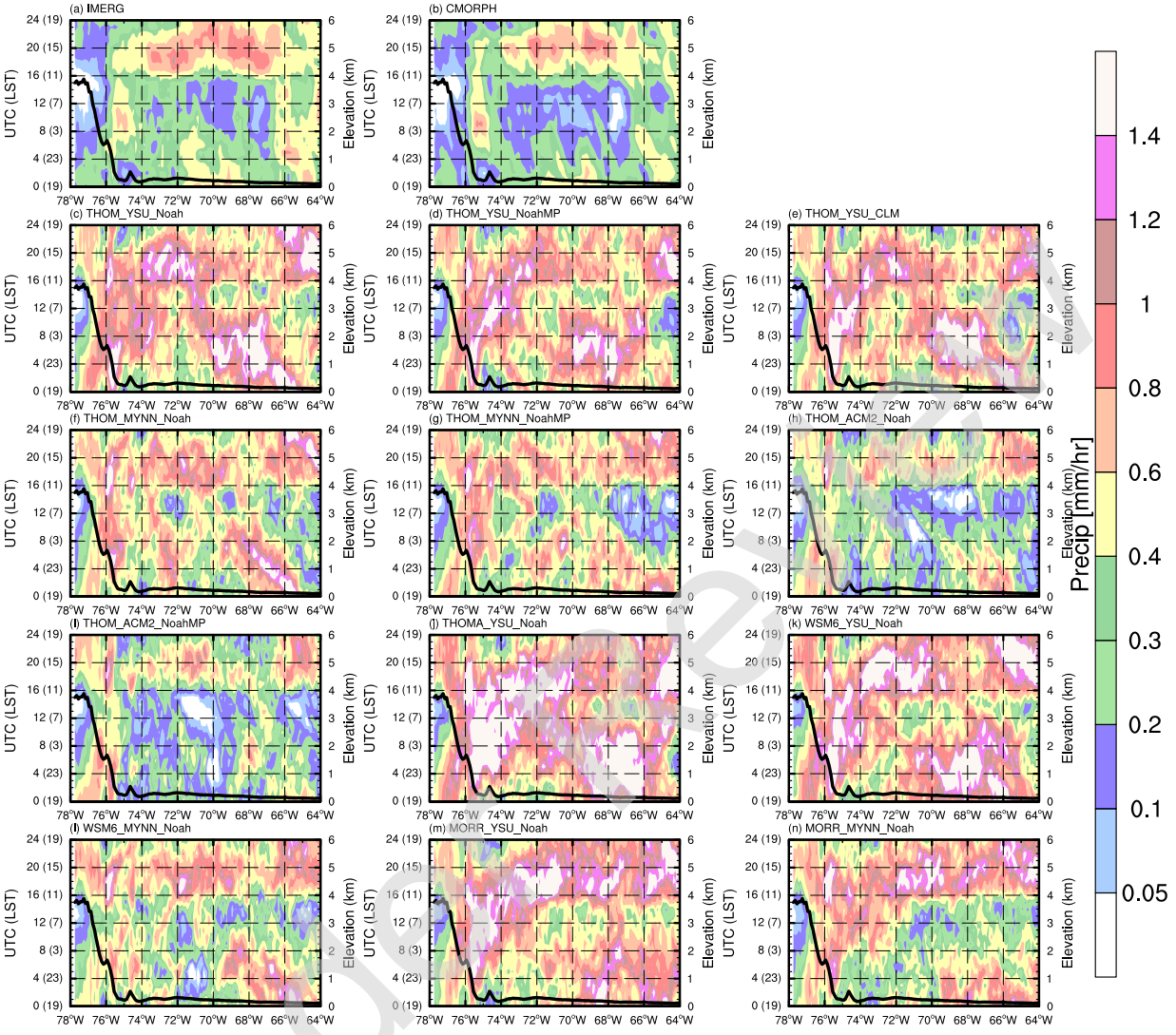

354 FIG. 7. Hovmöller diagrams of diurnal precipitation (shaded, mm h^{-1}) for the region marked by the white
355 rectangle shown in Fig. 2 from (a) IMERG, (b) CMORPH, and (c–n) WRF simulations using different physics
356 schemes in February 2019. The black curve in each panel represents meridionally-averaged terrain elevation
357 (km) in the region marked by the white rectangle shown in Fig. 2. The left Y-axis is for the Hovmöller diagram
358 and represents the time in UTC outside the parentheses and in the approximate Local Standard Time (LST =
359 UTC − 5 h, based on the longitude of 75°W) in the parentheses. The right Y-axis is for the terrain elevation.

369 results in this study are more sensitive to the PBL scheme than the MP and LSM schemes. It is
370 similar to the result of Kouadio et al. (2020), which revealed a stronger impact of PBL than MP

with the better performance of ACM2 non-local PBL scheme when simulating rainfall distribution over the Guinean coast and surroundings. Meroni et al. (2021) found PBL scheme has a greater impact than MP on the structure and distribution of heavy rainfall in the African continent. Prein et al. (2022) also indicated mesoscale convective systems in the central US are more sensitive to MP while PBL schemes are more influential in Brazil. Thus, differences among the simulations using different PBL schemes are further investigated in the next section.

c. Differences from PBL schemes

To examine the differences in the simulations due to using different PBL schemes, three simulations, i.e., THOM_YSU_Noah, THOM_MYNN_Noah, and THOM_ACM2_Noah that differ only in the PBL scheme used, are selected for further analysis. Because the low-level wind field is crucial to moisture transport and convection triggering, mean wind vectors at 925 hPa from ERA5 and the difference between the three simulations and ERA5 in February 2019 are displayed in Figs. 8a1–d1. From mean winds in Fig. 8a1, northerly winds prevail at 925 hPa along the Andes. The prevailing northerly winds combined with the notches of terrain result in the four precipitation hotspots along the Andes (Fig. 2). The differences in mean winds between simulated and ERA5 winds (Figs. 8b1–d1) are smaller than 1 m s^{-1}, indicating the simulated mean winds in THOM_YSU_Noah, THOM_MYNN_Noah, and THOM_ACM2_Noah are consistent with ERA5. Our preliminary tests (not shown) indicate that it is mainly associated with spectral nudging used in the 15-km domain, which makes simulated large-scale circulations consistent with those of ERA5.

From the diurnal deviation wind vectors shown in Figs. 8a2–d2, the simulations capture the evolution of deviation wind vectors well, which are consistent with that of ERA5, while the amplitudes of deviation winds are relatively large in the simulations, especially in THOM_YSU_Noah. The evolution of daily deviation winds can mostly be explained by the Blackadar inertial oscillation theory (Blackadar 1957), which is closely tied to boundary layer mixing and therefore influenced by the choice of PBL schemes. The critical roles of boundary layer inertial oscillations in producing nighttime/early morning precipitation in the rainy season in different regions have been demonstrated, such as the Asian monsoon region (Xue et al. 2018; Zhang et al. 2019; Chen 2020), Great Plains of the United States (Higgins et al. 1997; Trier et al. 2010), and east of the Andes (Saulo et al. 2000; Vernekar et al. 2003; Nicolini and Skabar 2011).

From 15 to 21 UTC (10–16 LST), the deviation wind vectors have a large change in terms of direction and magnitude, especially over the western Amazon Basin. The southerly deviation winds over the western Amazon Basin at 21 UTC (16 LST) are in the opposite direction to the mean winds, which reduces the full winds. It is associated with daytime boundary layer mixing. The magnitudes of deviation winds at 21 UTC (16 LST) are the largest in THOM_YSU_Noah, followed by THOM_MYNN_Noah, and are the smallest in THOM_ACM2_Noah. The magnitudes of deviation winds in THOM_ACM2_Noah are closer to ERA5 than THOM_YSU_Noah and THOM_MYNN_Noah (Figs. 8a2–d2). It means that using different PBL schemes for simulations can lead to differences in boundary layer vertical mixing and then the evolution of large-scale wind fields, which influences the convergence of low-level winds in terms of both intensity and spatial distribution. From the 925-hPa wind divergence at 03 UTC (22 LST) (Figs. 8a2–d2), there are larger areas with wind convergence (divergence of less than -1×10^{-5} s^{-1}) in THOM_YSU_Noah, which mainly covers the region of 10°–8°S, 70°–66°W over the western Amazon Basin. It can induce stronger and longer-lasting precipitation, which partially explains the stronger monthly and diurnal precipitation intensity and delayed precipitation peak time over the western Amazon Basin in THOM_YSU_Noah (as seen in Figs. 2, 5 and 7). This convergence is weaker in THOM_MYNN_Noah and THOM_ACM2_Noah (Figs. 8c2 and d2), which partially explains the weaker precipitation over the western Amazon Basin during 00–12 UTC (19–07 LST) (Fig. 7).

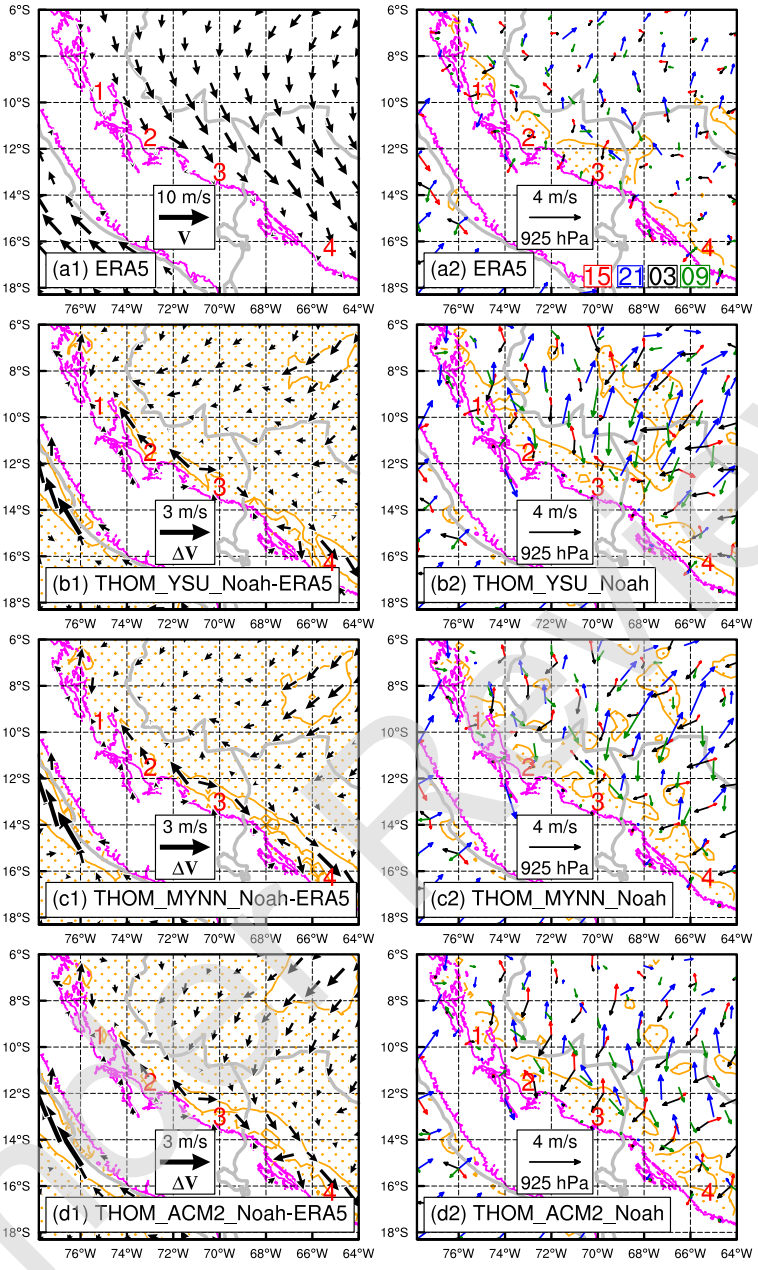

FIG. 8. (a1) Mean wind vectors at 925 hPa from ERA5 and difference between the simulations and ERA5 (WRF−ERA5) for (b1) THOM_YSU_Noah, (c1) THOM_MYNN_Noah, and (d1) THOM_ACM2_Noah in February 2019, respectively. (a2–d2) Deviation wind vectors (differences from daily mean wind vectors) at 925 hPa at 15 UTC [10 LST (Local Standard Time) at 75°W, red], 21 UTC (16 LST, blue), 03 UTC (22 LST, black), and 09 UTC (04 LST, green) in February 2019 for (a2) ERA5, (b2) THOM_YSU_Noah, (c2) THOM_MYNN_Noah, and (d2) THOM_ACM2_Noah, respectively. The orange dot-filled areas in b1–d1 indicate the regions with 925-hPa wind speed differences less than 1 m s^{-1}. The orange dot-filled areas in a2–d2 indicate the regions with 925-hPa wind divergence less than -1×10^{-5} s^{-1} at 03 UTC (22 LST). The magenta contour in each panel represents 1-km terrain elevation.

To examine the differences in vertical dynamic and thermodynamic structures, the vertical cross sections of meridionally-averaged and zonally-averaged equivalent potential temperature (θ_e), rainwater mixing ratio (Q_r), and wind vectors are shown in Figs. 9 and 10 respectively. At 15 UTC (10 LST), the vertical gradient of θ_e is larger in THOM_YSU_Noah and THOM_MYNN_Noah than that in THOM_ACM2_Noah, where θ_e increases from 344 to over 352 K from 2 km to surface in THOM_YSU_Noah and THOM_MYNN_Noah, while it increases from 344 to ~350 K in THOM_ACM2_Noah (Figs. 9a1–c1 and 10a1–c1). Therefore, more warm, moist energy exists in the lower levels in THOM_YSU_Noah and THOM_MYNN_Noah than that in THOM_ACM2_Noah. The horizontal winds in the upper levels are mainly easterly (Figs. 9a1–c1), while the horizontal winds in the lower levels are dominated by northerly winds (Figs. 10a1–c1). The Q_r over the western Amazon Basin is larger in THOM_YSU_Noah which can be over 0.08 g kg^{-1}, followed by THOM_MYNN_Noah, and the least in THOM_ACM2_Noah (Figs. 9a1–c1), which are consistent with the differences in precipitation among the three simulations (Figs. 7c, f and h).

At 21 UTC (16 LST), θ_e in the lower levels increases in all three simulations, to over 354 K near surface in THOM_YSU_Noah and THOM_MYNN_Noah, and to ~352 K in THOM_ACM2_Noah (Figs. 9a2–c2 and 10a2–c2), which is mainly associated with solar radiative heating in the daytime. The low-level v winds weaken at 21 UTC (16 LST) (Figs. 10a2–c2) compared to those at 15 UTC (10 LST) (Figs. 10a1–c1), which is mainly associated with the daytime vertical mixing process (consistent with those shown in Fig. 8). The Q_r in THOM_YSU_Noah is larger than that in THOM_MYNN_Noah, resulting in stronger precipitation (Fig. 7c).

From 03–09 UTC (22–04 LST)), there are more obvious convergence of u and v winds below 4 km, and more warm, moist energy release in THOM_YSU_Noah (Figs. 9a3–a4 10a3–a4, and also 8b2), associated with faster decreasing of θ_e, especially in the region of (10°–8°S, 70°–66°W). Thus, the Q_r is larger and precipitation is stronger in THOM_YSU_Noah (Figs. 7c, 9a3–a4, and 10a3–a4). The convergence of u and v winds below 4 km are weaker in THOM_MYNN_Noah (Figs. 9b3–b4, 10b3–b4, and also Fig. 8c2). Although there is also high θ_e in the low levels in THOM_MYNN_Noah, weaker wind convergence leads to less warm, moist energy release, resulting in less Q_r and weaker precipitation in THOM_MYNN_Noah (Figs. 7f, 9b3–b4, and 10b3–b4). There are divergences of u and v winds below 4 km over the western Amazon Basin,

and θ_e is generally lower in THOM_ACM2_Noah, leading to lesser Q_r and weaker precipitation (Figs. 7f, 8d2, 9c3–c4, and 10c3–c4).

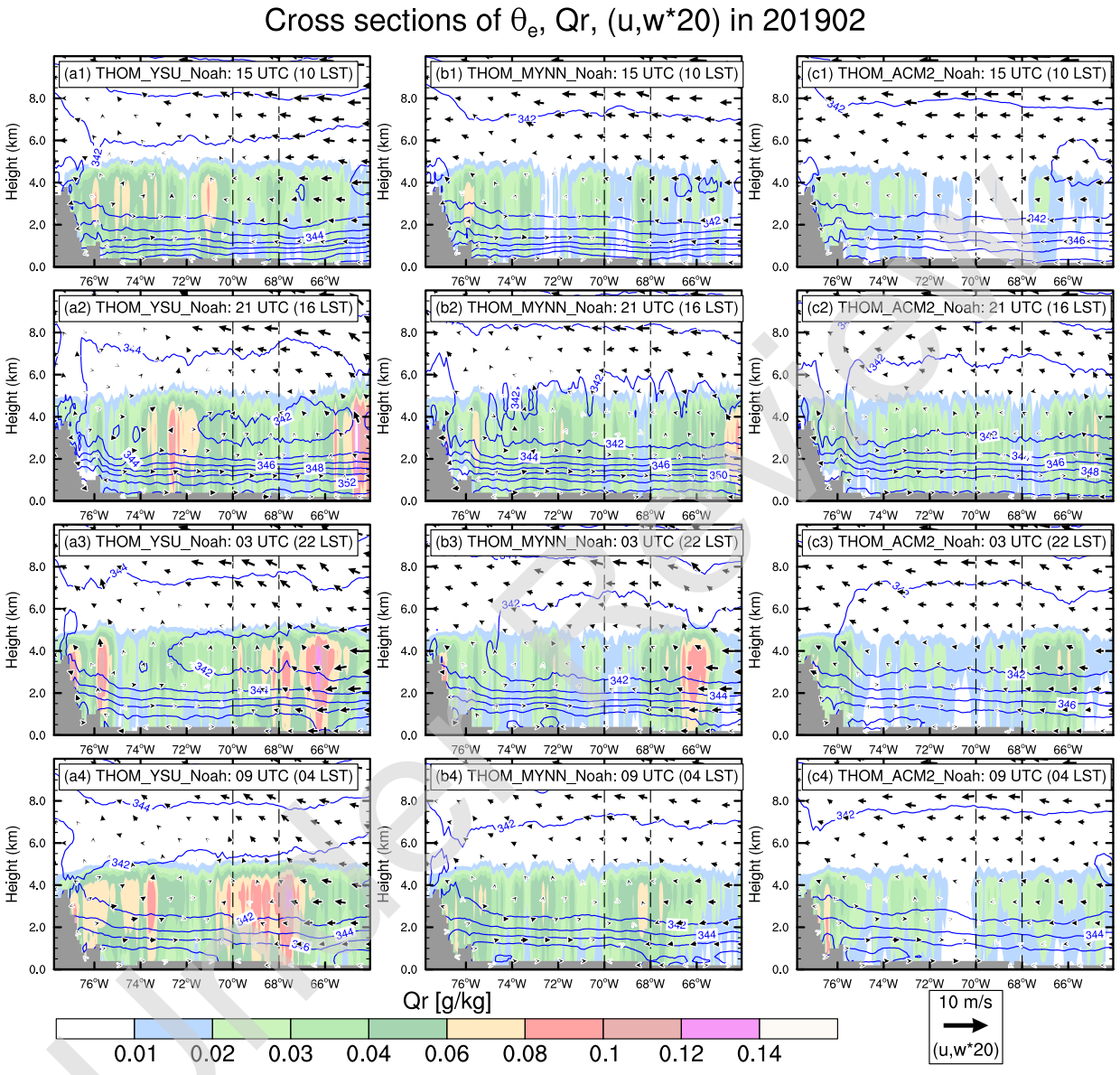

FIG. 9. Vertical cross sections of meridionally-averaged equivalent potential temperature (θ_e, K, blue contours in 2-K intervals), rainwater mixing ratio (Q_r, shaded, g kg^{-1}), and wind vectors (u, $w \times 20$) for the region of (10°–8°S, 78°–64°W) shown in Fig. 5 at (a1–c1) 15 UTC (10 LST), (a2–c2) 21 (16 LST), (a3–c3) 03 (22 LST), and (a4–c4) 09 UTC (04 LST) in (a1–a4) THOM_YSU_Noah, (b1–b4) THOM_MYNN_Noah, and (c1–c4) THOM_ACM2_Noah in February 2019, respectively. The gray shaded area in each panel represents the missing value due to the terrain.

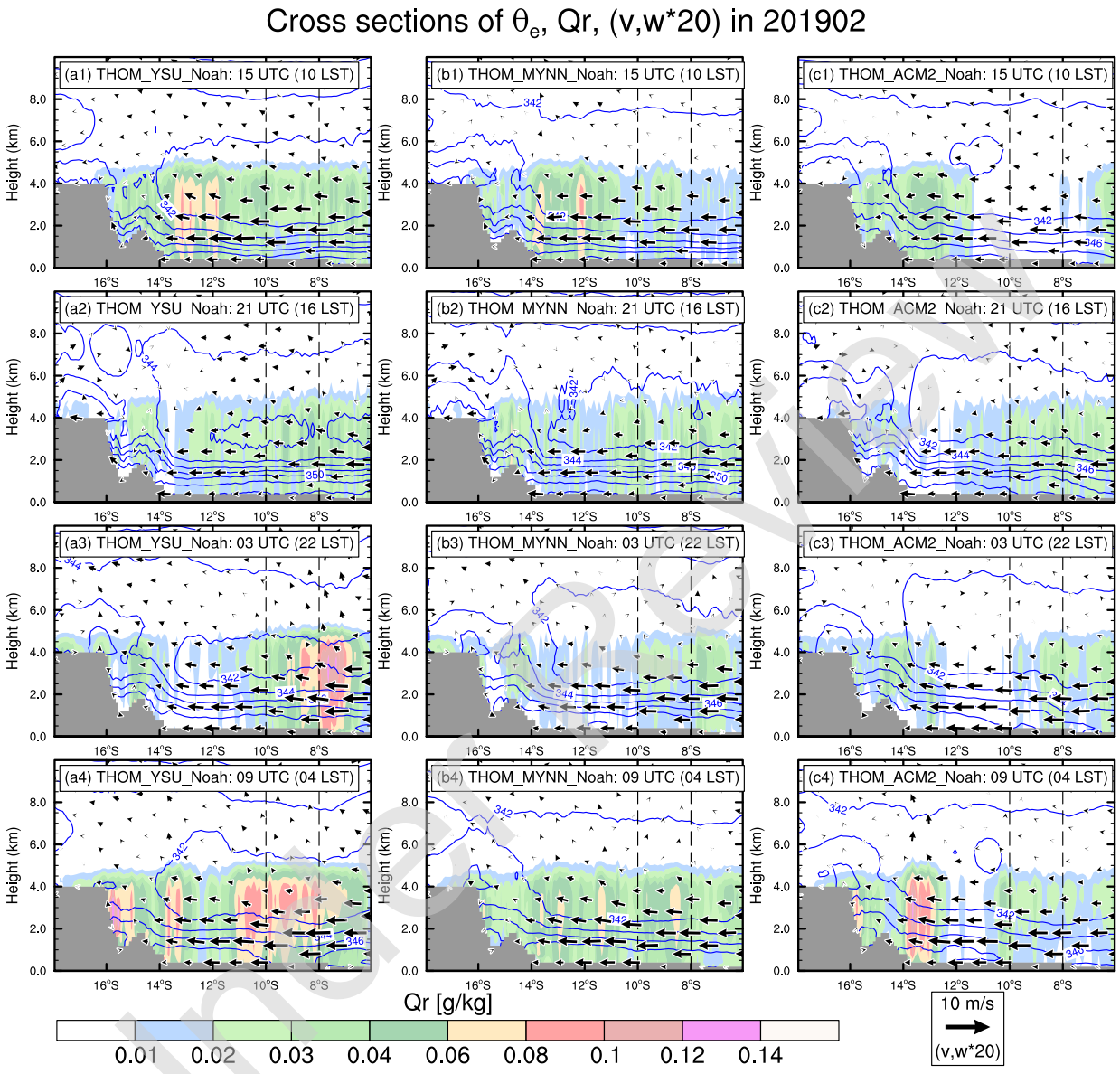

FIG. 10. Vertical cross sections of zonally-averaged equivalent potential temperature (θ_e, K, blue contours in 2-K intervals), rainwater mixing ratio (Q_r, shaded, g kg^{-1}), and wind vectors (v, $w \times 20$) for the region of (18°–6°S, 70°–68°W) shown in Fig. 5 at (a1–c1) 15 UTC (10 LST), (a2–c2) 21 UTC (16 LST), (a3–c3) 03 (22 LST), and (a4–c4) 09 UTC (04 LST) in (a1–a4) THOM_YSU_Noah, (b1–b4) THOM_MYNN_Noah, and (c1–c4) THOM_ACM2_Noah in February 2019, respectively. The gray shaded area in each panel represents the missing value due to the terrain.

To further examine the differences in PBL structures in the three simulations, time-height sections of averaged horizontal wind speeds (wspd), potential temperature (θ), and specific humidity (q_v) in the region of (10°–8°S, 70°–68°W) in THOM_YSU_Noah, THOM_MYNN_Noah, and THOM_ACM2_Noah in February 2019 are displayed in Fig. 11. To see their evolution more clearly, differences in v winds which dominate the horizontal winds (Figs. 8 and 10), θ, and q_v between current and previous hours are also plotted in Fig. 12 and represented as Δv, $\Delta\theta$, and Δq_v, respectively. The evolution of θ and q_v in the three simulations are similar in both daytime and nighttime (Figs. 11b1–b3 and c1–c3), while the vertical mixing of thermodynamics is stronger in THOM_YSU_Noah in the daytime with $\Delta\theta$ of over 0.4 K beyond the boundary layer top (Fig. 12b1). The higher θ and q_v in THOM_YSU_Noah and THOM_MYNN_Noah, where θ and q_v are respectively more than 303 K and 17 g kg^{-1} near the surface during the daytime (Figs. 12b1–b3 and c1–c3), are consistent with the higher θ_e in THOM_YSU_Noah and THOM_MYNN_Noah than THOM_ACM2_Noah (Figs. 9a1–c2).

There are larger differences in wspd evolution among the three simulations especially in the nighttime (Figs. 11a1–a3). With the development of the boundary layer in the daytime (06–18 LST), wspd increases and its vertical gradient within the boundary layer in THOM_YSU_Noah (from less than 3 m s^{-1} near the surface to less than 4 m s^{-1} at the boundary layer top at 16 LST) is smaller than those in THOM_MYNN_Noah (from less than 3 m s^{-1} near the surface to ~4 m s^{-1} at the boundary layer top at 16 LST) and THOM_ACM2_Noah (from less than 3 m s^{-1} near the surface to larger than 4 m s^{-1} at the boundary layer top at 16 LST) (Figs. 11a1–a3). It is consistent with the larger Δv (over 1 m s^{-1}) in THOM_YSU_Noah during 07–11 LST (Fig. 12a1), implying stronger vertical mixing of momentum within the boundary layer. After 15 LST, northerly winds start to develop below 3 km AGL in THOM_ACM2_Noah (Fig. 12a3), but it happens about 1 h later in THOM_YSU_Noah and 2-h later in THOM_MYNN_Noah (Figs. 12a1 and a2). However, the development of northerly winds lasts longer in THOM_YSU_Noah, in which $\Delta v < -0.2$ m s^{-1} and $\Delta v < -0.4$ m s^{-1} can reach around 03 LST and beyond 00 LST respectively, while $\Delta v < -0.2$ m s^{-1} in THOM_MYNN_Noah and THOM_ACM2_Noah do not exist after 23 LST (Figs. 12a1–a3). Therefore, stronger low-level jet develops in THOM_YSU_Noah with maximum wspd over 7 m s^{-1} between 0.5–1.75 km AGL during the nighttime (Fig. 11a1), which is consistent with the stronger precipitation during 04–08 UTC (23–03 LST) in the examined

region in THOM_YSU_Noah (Fig. 7c). The different precipitation peak time over the western Amazon Basin among the three simulations (Figs. 5c, f, and h) may be associated with the different developments of this low-level jet in the nighttime, which results from the different boundary layer mixing strength in the three PBL schemes. Martinez et al. (2022) also indicated that the choice of PBL schemes strongly impacts the development of low-level jets and subsequent precipitation in their three-month simulations over the Colombian Andes region at a 12-km grid spacing. Martinez et al. (2022) also revealed that the simulation using YSU scheme resulted in stronger low-level jets compared to the simulation using MYNN scheme. These findings underscore the importance of selecting appropriate PBL schemes to improve precipitation simulation and forecasting in complex terrain regions.

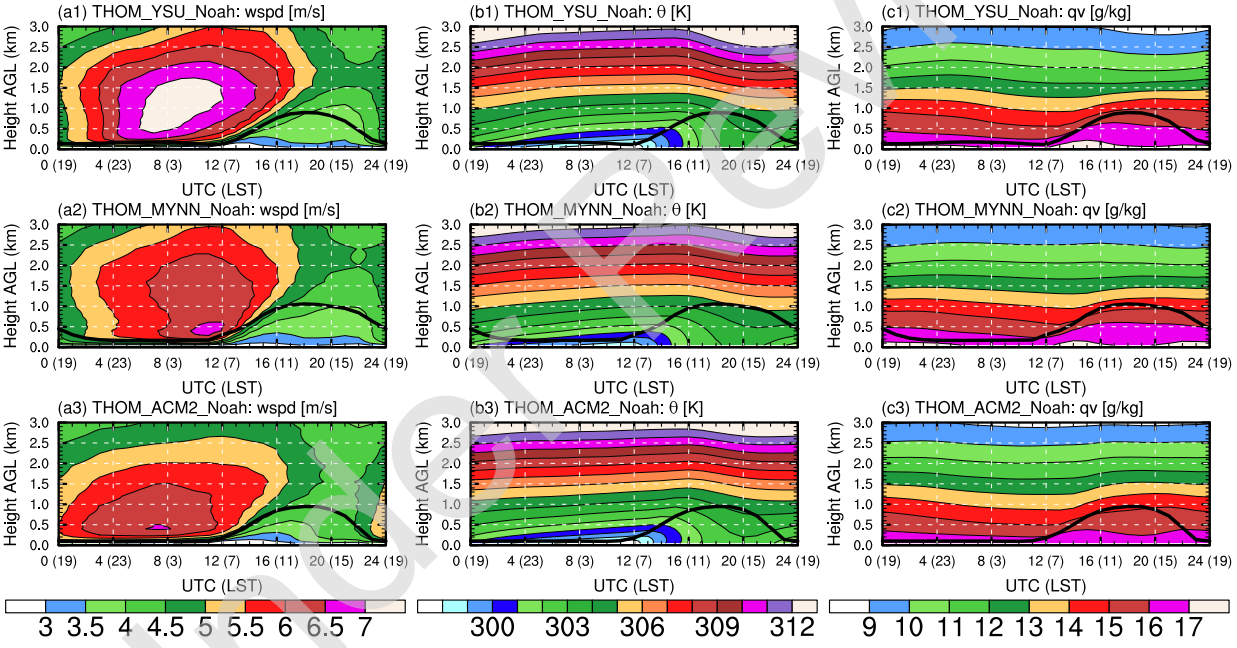

FIG. 11. Time-height sections of averaged (a1–a3) horizontal wind speeds (wspd, m s^{-1}), (b1–b3) potential temperature (θ, K), and (c1–c3) specific humidity (q_v, g kg^{-1}) in the region of (10°–8°S, 70°–68°W) in (a1–c1) THOM_YSU_Noah, (a2–c2) THOM_MYNN_Noah, and (a3–c3) THOM_ACM2_Noah in February 2019, respectively. The black thick curves indicate averaged boundary layer height in each simulation. X-axis represents the time in UTC outside the parentheses and in LST (Local Standard Time, here LST = UTC − 5 h in the examined region) in the parentheses. Y-axis represents the height above ground level (km) in each panel.

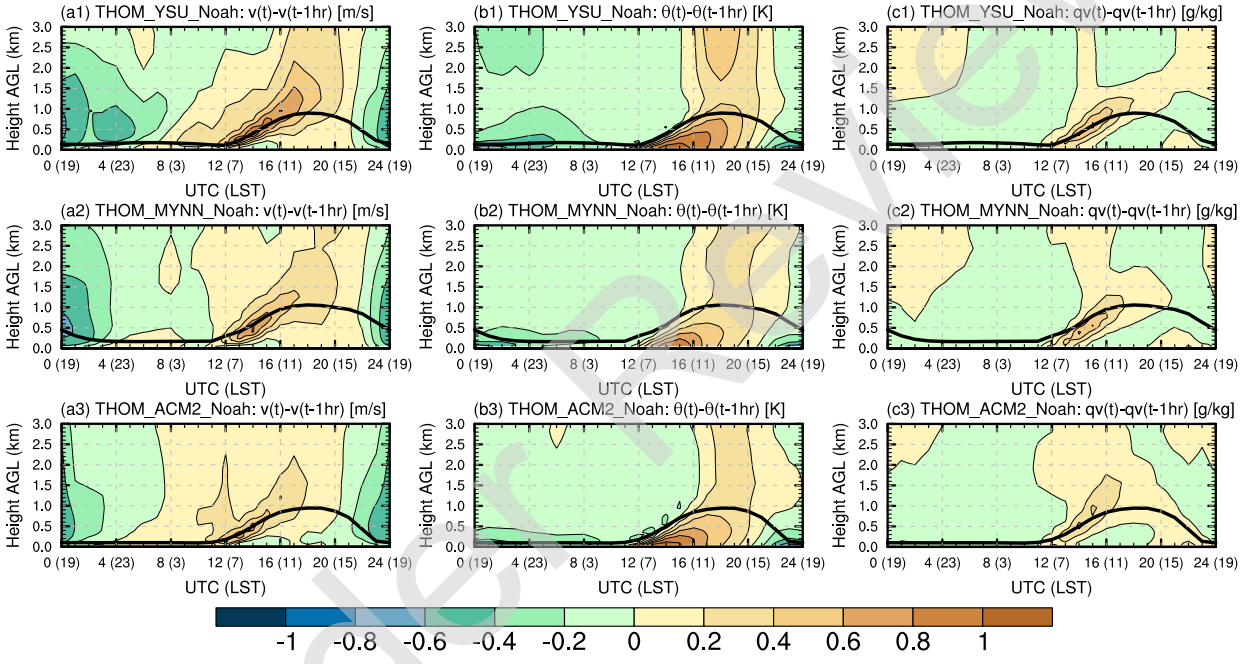

FIG. 12. As in Fig. 11 but for the differences in v winds, potential temperature (θ), and specific humidity (q_v) between current hour and previous hour, referred to as (a1–a3) Δv, (b1–b3) $\Delta\theta$, and (c1–c3) Δq_v, respectively.

The instantaneous time tendencies of v winds, θ, and q_v due to PBL parameterization shown in Fig. 13 have similar patterns to the difference fields in Fig. 12 in the morning (06–12 LST), but different patterns appear after 12 LST. It suggests that the accumulative effects of PBL parameterization start to influence the PBL processes in the afternoon. PBL parameterizations influence momentum, heat, moisture, and cloud fields, and there are also complex interactions among these fields. Differences in the strength of daytime boundary layer mixing and nighttime decay would affect the development of nocturnal low-level jets, transport of boundary layer moisture and momentum, low-level wind convergence, and final precipitation. The strength and distribution of precipitation would then have feedback to the low-level circulations, which then again affect precipitation. Thus, it is difficult to link the accumulative effects to the tendencies due to PBL parameterization, in particular the large-scale fields have been changed by the accumulative effects of PBL parameterization (Fig. 11). To examine the attribution of differences among the three simulations using different PBL schemes, especially the low-level jets in the nighttime, sensitivity experiments examining different terms (e.g., the local, non-local mixing, and boundary layer top entrainment terms) in the PBL schemes need to be performed. However, this aspect is outside the scope of this paper and has been thoroughly investigated in our subsequent publication (Hu et al. 2023), which indicated that the free-troposphere mixing in the presence of clouds appears to be the key factor in explaining the substantial difference in simulated precipitation between THOM_YSU_Noah and THOM_ACM2_Noah.

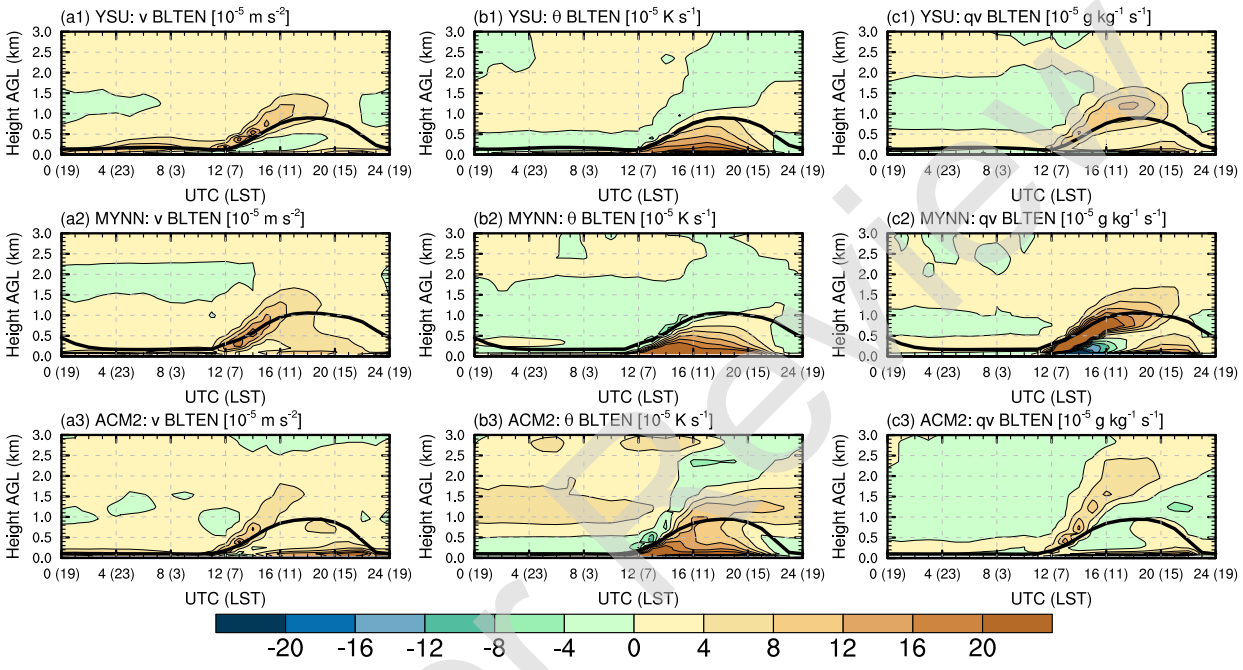

FIG. 13. Time-height sections of averaged instantaneous tendencies due to PBL parameterization of (a1–a3) v wind (10^{-5} m s^{-2}), (b1–b3) potential temperature (10^{-5} K s^{-1}), and (c1–c3) specific humidity (10^{-5} g kg^{-1} s^{-1}) in the region of (10°–8°S, 70°–68°W) in (a1–c1) THOM_YSU_Noah, (a2–c2) THOM_MYNN_Noah, and (a3–c3) THOM_ACM2_Noah in February 2019, respectively. The black thick curves indicate averaged boundary layer height in each simulation. X-axis represents the time in UTC outside the parentheses and in LST (Local Standard Time, here LST = UTC − 5 h in the examined region) in the parentheses. Y-axis represents the height above ground level (km) in each panel.

4. Summary

To help choose the best physics configuration of a WRF-based regional climate model for performing dynamic downscaling of future climate for the Peruvian Central Andes region at a convection-permitting resolution, twelve two-month-long simulations using the WRF model with different physics parameterization schemes are performed during January and February 2019 in the austral summer. The WRF model is run with a 15-km grid covering entire South America forced at the lateral boundaries by hourly ERA5 reanalysis data and a one-way nested 3-km grid covering the Peruvian central Andes region. The monthly and diurnal precipitation in the 3-km simulations are evaluated using rain gauge data in Peru and three higher-temporal-resolution global precipitation products, i.e., IMERG, CMORPH, and MSWEP. The major results are summarized as follows.

(1) Through comparing the monthly precipitation of the three global precipitation datasets and simulations to the rain gauge data, MSWEP shows the smallest RMSE with a positive bias, and IMERG and CMORPH generally underestimate the monthly precipitation. All twelve simulations generally overestimate the precipitation, where the simulation using the Thompson microphysics scheme, ACM2 PBL scheme and Noah land surface model has the smallest mean bias and RMSE, and the simulation using Thompson aerosol-aware scheme, YSU PBL scheme and Noah land surface model has the largest mean bias and RMSE.

(2) All simulations successfully capture the four precipitation hotspots associated with the prevailing winds and terrain features along the east slope of the Peruvian Central Andes. The simulated precipitation is the most sensitive to the PBL scheme, followed by the microphysics scheme, and is least sensitive to the LSM scheme. The simulated precipitation is generally stronger in the simulations using YSU PBL scheme than MYNN and ACM2 schemes. The simulation using Thompson scheme, ACM2 PBL scheme and Noah land surface model is the closest to the precipitation of IMERG and MSWEP.

(3) Based on IMERG and CMORPH, diurnal precipitation peak time is mainly in the afternoon (~14–19 LST) over the Peruvian Central Andes for terrain elevations higher than 1 km, in the early morning (~0–6 LST) along the east slope of the Peruvian Central Andes for terrain elevations around 1 km, and between ~14–19 LST over the western Amazon Basin to the east of the Peruvian Central Andes. All simulations successfully capture the precipitation peak time over the Peruvian

Central Andes and also along its east slope, while large differences exist in the precipitation peak time over the western Amazon Basin with about 4–8-h delay in simulations using YSU PBL scheme. The simulations using ACM2 PBL scheme have a smaller delay.

(4) Different PBL schemes can lead to differences in the evolution of large-scale low-level wind fields, which influences the intensity and spatial distribution of low-level wind convergence. The θ_e within PBL is generally higher during the daytime in simulations using YSU and MYNN schemes than in simulations using ACM2 scheme, which is consistent with the stronger precipitation in simulations using YSU and MYNN schemes. Obvious differences exist in the development of low-level jets during nighttime due to accumulative effects of different PBL schemes. The stronger and longer-lasting low-level jets in simulation using YSU scheme are consistent with the delayed precipitation peak time over the western Amazon Basin.

These results provide guidance on the optimal configuration of regional climate models for future climate dynamic downscaling for the Peruvian Central Andes region. Based on the testing results, the YSU PBL scheme produces the highest bias in simulated precipitation as well as the most delay in diurnal precipitation peak time. The ACM2 PBL scheme appears to be the preferred choice while MYNN PBL scheme also performs reasonably well. However, simulations over longer periods and spanning multiple years should be performed to make sure that such relative performances carry to the regional climate simulation application. We are currently running two configurations using Thompson microphysics and Noah LSM, combined with ACM2 and MYNN PBL schemes respectively, and the results will be reported in the future. The configuration with better performance will be used for future convection-permitting regional climate simulations for the Peruvian Central Andes region.

Acknowledgments. This project was primarily supported by grant No. 20163646499 from the Universidad Nacional de San Agustín de Arequipa (UNSA) of Peru through the IREES/LASI Global Change and Human Health Institute. Supplementary funding was provided by the Weathernews Chair funds. The authors acknowledge the Texas Advanced Computing Center (TACC) at the University of Texas at Austin (http://www.tacc.utexas.edu) for providing HPC resources through XSEDE allocation TG-ATM160014 that are used for the simulations. The authors also acknowledge high-performance computing support from Cheyenne (https://doi.org/10.5065/D6RX99HX) provided by NCAR's Computational and Information Systems Laboratory. NCAR is sponsored by the National Science Foundation. Some data processing was performed at the University of Oklahoma (OU) Supercomputing Center for Education and Research (OSCER).

Data availability statement. ERA5 reanalysis data are available at https://doi.org/10.5065/BH6N-5N20. GPM IMERG Final Precipitation dataset is available at https://doi.org/10.5067/GPM/IMERGDF/DAY/06 (last access: 12 November 2020). CMORPH dataset is available at https://ftp.cpc.ncep.noaa.gov/precip/CMORPH_V1.0/CRT/8km-30min (last access: 12 November 2020). MSWEP dataset is available at http://www.gloh2o.org/mswep (last access: 17 July 2021). The rain gauge data are available at https://piscoprec.github.io/webPISCO/en/raingauges (last access: 18 July 2021). The model outputs are too large to be publicly archived. Please contact the corresponding author for more information.

References

Adinolfi, M., M. Raffa, A. Reder, and P. Mercogliano, 2020: Evaluation and expected changes of summer precipitation at convection permitting scale with cosmo-clm over alpine space. *Atmosphere*, **12 (1)**, 54, https://doi.org/10.3390/atmos12010054.

Afonso, J. M. d. S., D. A. Vila, M. A. Gan, D. P. Quispe, N. d. J. d. C. Barreto, J. H. Huamán Chinchay, and R. S. A. Palharini, 2020: Precipitation diurnal cycle assessment of satellite-based estimates over brazil. *Remote Sensing*, **12 (14)**, 2339, https://doi.org/10.3390/rs12142339.

Ambrizzi, T., M. S. Reboita, R. P. da Rocha, and M. Llopart, 2019: The state of the art and fundamental aspects of regional climate modeling in south america. *Annals of the new york academy of sciences*, **1436 (1)**, 98–120, https://doi.org/10.1111/nyas.13932.

Avila-Diaz, A., G. Abrahão, F. Justino, R. Torres, and A. Wilson, 2020: Extreme climate indices in brazil: evaluation of downscaled earth system models at high horizontal resolution. *Climate Dynamics*, **54 (11-12)**, 5065–5088, https://doi.org/10.1007/s00382-020-05272-9.

Aybar, C., C. Fernández, A. Huerta, W. Lavado, F. Vega, and O. Felipe-Obando, 2020: Construction of a high-resolution gridded rainfall dataset for peru from 1981 to the present day. *Hydrological Sciences Journal*, **65 (5)**, 770–785, https://doi.org/10.1080/02626667.2019.1649411.

Ban, N., J. Schmidli, and C. Schär, 2014: Evaluation of the convection-resolving regional climate modeling approach in decade-long simulations. *Journal of Geophysical Research: Atmospheres*, **119 (13)**, 7889–7907, https://doi.org/10.1002/2014JD021478.

Beck, H. E., E. F. Wood, M. Pan, C. K. Fisher, D. G. Miralles, A. I. Van Dijk, T. R. McVicar, and R. F. Adler, 2019: Mswep v2 global 3-hourly 0.1 precipitation: methodology and quantitative assessment. *Bulletin of the American Meteorological Society*, **100 (3)**, 473–500, https://doi.org/10.1175/BAMS-D-17-0138.1.

Berthou, S., E. J. Kendon, S. C. Chan, N. Ban, D. Leutwyler, C. Schär, and G. Fosser, 2020: Pan-european climate at convection-permitting scale: a model intercomparison study. *Climate Dynamics*, **55 (1)**, 35–59, https://doi.org/10.1007/s00382-018-4114-6.

Berthou, S., D. P. Rowell, E. J. Kendon, M. J. Roberts, R. A. Stratton, J. A. Crook, and C. Wilcox, 2019: Improved climatological precipitation characteristics over west africa at convection-permitting scales. *Climate Dynamics*, **53 (3)**, 1991–2011, https://doi.org/10.1007/s00382-019-04759-4.

Bettolli, M. L., and Coauthors, 2021: The cordex flagship pilot study in southeastern south america: a comparative study of statistical and dynamical downscaling models in simulating daily extreme precipitation events. *Climate Dynamics*, **56**, 1589–1608, https://doi.org/10.1007/s00382-020-05549-z.

Blackadar, A. K., 1957: Boundary layer wind maxima and their significance for the growth of nocturnal inversions. *Bulletin of the American Meteorological Society*, **38 (5)**, 283–290, https://doi.org/10.1175/1520-0477-38.5.283.

Chan, S. C., E. J. Kendon, S. Berthou, G. Fosser, E. Lewis, and H. J. Fowler, 2020: Europe-wide precipitation projections at convection permitting scale with the unified model. *Climate Dynamics*, **55 (3)**, 409–428, https://doi.org/10.1007/s00382-020-05192-8.

Chavez, S. P., Y. Silva, and A. P. Barros, 2020: High-elevation monsoon precipitation processes in the central andes of peru. *Journal of Geophysical Research: Atmospheres*, **125 (24)**, e2020JD032 947, https://doi.org/10.1029/2020JD032947.

Chavez, S. P., and K. Takahashi, 2017: Orographic rainfall hot spots in the andes-amazon transition according to the trmm precipitation radar and in situ data. *Journal of Geophysical Research: Atmospheres*, **122 (11)**, 5870–5882, https://doi.org/10.1002/2016JD026282.

Chen, G., 2020: Diurnal cycle of the asian summer monsoon: Air pump of the second kind. *Journal of Climate*, **33 (5)**, 1747–1775, https://doi.org/10.1175/JCLI-D-19-0210.1.

Chen, M., and Coauthors, 2022: Cross-examining precipitation products by rain gauge, remote sensing, and wrf simulations over a south american region across the pacific coast and andes. *Atmosphere*, **13 (10)**, 1666, https://doi.org/10.3390/atmos13101666.

Chimborazo, O., and M. Vuille, 2021: Present-day climate and projected future temperature and precipitation changes in ecuador. *Theoretical and Applied Climatology*, **143 (3-4)**, 1581–1597, https://doi.org/10.1007/s00704-020-03483-y.

Ciarlo, J. M., and Coauthors, 2020: A new spatially distributed added value index for regional climate models: the euro-cordex and the cordex-core highest resolution ensembles. *Climate Dynamics*, 1–22, https://doi.org/10.1007/s00382-020-05400-5.

Coppola, E., and Coauthors, 2020: A first-of-its-kind multi-model convection permitting ensemble for investigating convective phenomena over europe and the mediterranean. *Climate Dynamics*, **55 (1)**, 3–34, https://doi.org/10.1007/s00382-018-4521-8.

da Silva, M. L., C. P. de Oliveira, C. M. Santos e Silva, and J. M. de Araújo, 2023: Dynamic downscaling of climate simulations and projected changes in tropical south america using regcm4. 7. *International Journal of Climatology*, https://doi.org/10.1002/joc.8035.

Dezfuli, A. K., C. M. Ichoku, G. J. Huffman, K. I. Mohr, J. S. Selker, N. Van De Giesen, R. Hochreutener, and F. O. Annor, 2017: Validation of imerg precipitation in africa. *Journal of Hydrometeorology*, **18 (10)**, 2817–2825, https://doi.org/10.1175/JHM-D-17-0139.1.

Ek, M., K. Mitchell, Y. Lin, E. Rogers, P. Grunmann, V. Koren, G. Gayno, and J. Tarpley, 2003: Implementation of noah land surface model advances in the national centers for environmental prediction operational mesoscale eta model. *Journal of Geophysical Research: Atmospheres*, **108 (D22)**, https://doi.org/10.1029/2002JD003296.

Espinoza, J. C., S. Chavez, J. Ronchail, C. Junquas, K. Takahashi, and W. Lavado, 2015: Rainfall hotspots over the southern tropical andes: Spatial distribution, rainfall intensity, and relations with large-scale atmospheric circulation. *Water Resources Research*, **51 (5)**, 3459–3475, https://doi.org/10.1002/2014WR016273.

Falco, M., A. F. Carril, L. Z. Li, C. Cabrelli, and C. G. Menéndez, 2020: The potential added value of regional climate models in south america using a multiresolution approach. *Climate Dynamics*, **54 (3)**, 1553–1569, https://doi.org/10.1007/s00382-019-05073-9.

Feng, Z., L. R. Leung, R. A. Houze Jr, S. Hagos, J. Hardin, Q. Yang, B. Han, and J. Fan, 2018: Structure and evolution of mesoscale convective systems: Sensitivity to cloud microphysics in convection-permitting simulations over the united states. *Journal of Advances in Modeling Earth Systems*, **10 (7)**, 1470–1494, https://doi.org/10.1029/2018MS001305.

Feser, F., B. Rockel, H. von Storch, J. Winterfeldt, and M. Zahn, 2011: Regional climate models add value to global model data: a review and selected examples. *Bulletin of the American Meteorological Society*, **92 (9)**, 1181–1192, https://doi.org/10.1175/2011BAMS3061.1.

Fosser, G., E. J. Kendon, D. Stephenson, and S. Tucker, 2020: Convection-permitting models offer promise of more certain extreme rainfall projections. *Geophysical Research Letters*, **47 (13)**, e2020GL088 151, https://doi.org/10.1029/2020GL088151.

Fosser, G., S. Khodayar, and P. Berg, 2015: Benefit of convection permitting climate model simulations in the representation of convective precipitation. *Climate Dynamics*, **44 (1-2)**, 45–60, https://doi.org/10.1007/s00382-014-2242-1.

Fumière, Q., M. Déqué, O. Nuissier, S. Somot, A. Alias, C. Caillaud, O. Laurantin, and Y. Seity, 2020: Extreme rainfall in mediterranean france during the fall: added value of the cnrm-arome convection-permitting regional climate model. *Climate Dynamics*, **55 (1)**, 77–91, https://doi.org/10.1007/s00382-019-04898-8.

Gao, X., Y. Xu, Z. Zhao, J. Pal, and F. Giorgi, 2006: On the role of resolution and topography in the simulation of east asia precipitation. *Theoretical and Applied Climatology*, **86 (1)**, 173–185, https://doi.org/10.1007/s00704-005-0214-4.

Gao, Y., F. Chen, and Y. Jiang, 2020: Evaluation of a convection-permitting modeling of precipitation over the tibetan plateau and its influences on the simulation of snow-cover fraction. *Journal of Hydrometeorology*, **21 (7)**, 1531–1548.

Gao, Y., L. R. Leung, C. Zhao, and S. Hagos, 2017: Sensitivity of us summer precipitation to model resolution and convective parameterizations across gray zone resolutions. *Journal of Geophysical Research: Atmospheres*, **122 (5)**, 2714–2733, https://doi.org/10.1002/2016JD025896.

Gensini, V. A., A. M. Haberlie, and W. S. Ashley, 2022: Convection-permitting simulations of historical and possible future climate over the contiguous united states. *Climate Dynamics*, 1–18, https://doi.org/10.1007/s00382-022-06306-0.

Giorgi, F., 2006: Regional climate modeling: Status and perspectives. *Journal de Physique IV (proceedings)*, EDP sciences, Vol. 139, 101–118, https://doi.org/10.1051/jp4:2006139008.

Giorgi, F., 2019: Thirty years of regional climate modeling: where are we and where are we going next? *Journal of Geophysical Research: Atmospheres*, **124 (11)**, 5696–5723, https://doi.org/10.1029/2018JD030094.

Giorgi, F., and G. T. Bates, 1989: The climatological skill of a regional model over complex terrain. *Monthly Weather Review*, **117 (11)**, 2325–2347, https://doi.org/10.1175/1520-0493(1989)117⟨2325:TCSOAR⟩2.0.CO;2.

González-Rojí, S. J., M. Messmer, C. C. Raible, and T. F. Stocker, 2022: Sensitivity of precipitation in the highlands and lowlands of peru to physics parameterization options in wrfv3. 8.1. *Geoscientific Model Development*, **15 (7)**, 2859–2879, https://doi.org/10.5194/gmd-15-2859-2022.

Guo, Z., J. Fang, X. Sun, J. Tang, Y. Yang, and J. Tang, 2020: Decadal long convection-permitting regional climate simulations over eastern china: evaluation of diurnal cycle of precipitation. *Climate Dynamics*, **54 (3)**, 1329–1349, https://doi.org/10.1007/s00382-019-05061-z.

Guo, Z., J. Fang, X. Sun, Y. Yang, and J. Tang, 2019: Sensitivity of summer precipitation simulation to microphysics parameterization over eastern china: Convection-permitting regional climate simulation. *Journal of Geophysical Research: Atmospheres*, **124 (16)**, 9183–9204, https://doi.org/10.1029/2019JD030295.

Gutowski Jr, W. J., and Coauthors, 2016: Wcrp coordinated regional downscaling experiment (cordex): a diagnostic mip for cmip6. https://doi.org/10.5194/gmd-9-4087-2016.

He, C., F. Chen, M. Barlage, C. Liu, A. Newman, W. Tang, K. Ikeda, and R. Rasmussen, 2019: Can convection-permitting modeling provide decent precipitation for offline high-resolution snowpack simulations over mountains? *Journal of Geophysical Research: Atmospheres*, **124 (23)**, 12 631–12 654, https://doi.org/10.1029/2019JD030823.

Hersbach, H., and Coauthors, 2020: The era5 global reanalysis. *Quarterly Journal of the Royal Meteorological Society*, **146 (730)**, 1999–2049, https://doi.org/10.1002/qj.3803.

Higgins, R., Y. Yao, E. Yarosh, J. E. Janowiak, and K. Mo, 1997: Influence of the great plains low-level jet on summertime precipitation and moisture transport over the central united states. *Journal of Climate*, **10 (3)**, 481–507, https://doi.org/10.1175/1520-0442(1997)010⟨0481:IOTGPL⟩2.0.CO;2.

Hodnebrog, Ø., B. Steensen, L. Marelle, K. Alterskjaer, S. Dalsøren, and G. Myhre, 2021: Understanding model diversity in future precipitation projections for south america. *Climate Dynamics*, 1–19, https://doi.org/10.1007/s00382-021-05964-w.

Hong, S.-Y., and J.-O. J. Lim, 2006: The wrf single-moment 6-class microphysics scheme (wsm6). *Asia-Pacific Journal of Atmospheric Sciences*, **42 (2)**, 129–151.

Hu, X.-M., M. Xue, R. A. McPherson, E. Martin, D. H. Rosendahl, and L. Qiao, 2018: Precipitation dynamical downscaling over the great plains. *Journal of Advances in Modeling Earth Systems*, **10 (2)**, 421–447, https://doi.org/10.1002/2017MS001154.

Hu, X.-M., and Coauthors, 2023: Effects of lower troposphere vertical mixing on simulated clouds and precipitation over the amazon during the wet season. *Journal of Geophysical Research-Atmospheres*, in revision, https://doi.org/10.22541/essoar.167458066.61800879/v1.

Huang, Y., Y. Wang, L. Xue, X. Wei, L. Zhang, and H. Li, 2020: Comparison of three microphysics parameterization schemes in the wrf model for an extreme rainfall event in the coastal metropolitan city of guangzhou, china. *Atmospheric Research*, **240**, 104 939, https://doi.org/10.1016/j.atmosres.2020.104939.

Huffman, G., E. Stocker, D. Bolvin, E. Nelkin, and J. Tan, 2019: Gpm imerg final precipitation l3 1 day 0.1 degree x 0.1 degree v06, edited by andrey savtchenko, greenbelt, md, goddard earth sciences data and information services center (ges disc). Accessed: [12 November 2020], https://doi.org/10.5067/GPM/IMERGDF/DAY/06.

Iacono, M. J., J. S. Delamere, E. J. Mlawer, M. W. Shephard, S. A. Clough, and W. D. Collins, 2008: Radiative forcing by long-lived greenhouse gases: Calculations with the aer radiative transfer models. *Journal of Geophysical Research: Atmospheres*, **113 (D13)**, https://doi.org/10.1029/2008JD009944.

Jiménez, P. A., J. Dudhia, J. F. González-Rouco, J. Navarro, J. P. Montávez, and E. García-Bustamante, 2012: A revised scheme for the wrf surface layer formulation. *Monthly Weather Review*, **140 (3)**, 898–918, https://doi.org/10.1175/MWR-D-11-00056.1.

Jones, C., 2019: Recent changes in the south america low-level jet. *Npj Climate and Atmospheric Science*, **2 (1)**, 20, https://doi.org/10.1038/s41612-019-0077-5.

Joyce, R. J., J. E. Janowiak, P. A. Arkin, and P. Xie, 2004: Cmorph: A method that produces global precipitation estimates from passive microwave and infrared data at high spatial and temporal resolution. *Journal of hydrometeorology*, **5 (3)**, 487–503, https://doi.org/10.1175/1525-7541(2004)005⟨0487:CAMTPG⟩2.0.CO;2.

Juckes, M., and Coauthors, 2020: The cmip6 data request (dreq, version 01.00. 31). *Geoscientific Model Development*, **13 (1)**, 201–224, https://doi.org/10.5194/gmd-13-201-2020.

Junquas, C., K. Takahashi, T. Condom, J.-C. Espinoza, S. Chávez, J.-E. Sicart, and T. Lebel, 2018: Understanding the influence of orography on the precipitation diurnal cycle and the associated

atmospheric processes in the central andes. *Climate dynamics*, **50**, 3995–4017, https://doi.org/10.1007/s00382-017-3858-8.

Junquas, C., and Coauthors, 2022: Regional climate modeling of the diurnal cycle of precipitation and associated atmospheric circulation patterns over an andean glacier region (antisana, ecuador). *Climate Dynamics*, **58 (11-12)**, 3075–3104, https://doi.org/10.1007/s00382-021-06079-y.

Kanamitsu, M., and H. Kanamaru, 2007: Fifty-seven-year california reanalysis downscaling at 10 km (card10). part i: System detail and validation with observations. *Journal of Climate*, **20 (22)**, 5553–5571, https://doi.org/10.1175/2007JCLI1482.1.

Karki, R., L. Gerlitz, U. Schickhoff, T. Scholten, J. Böhner, and Coauthors, 2017: Quantifying the added value of convection-permitting climate simulations in complex terrain: a systematic evaluation of wrf over the himalayas. *Earth System Dynamics*, **8 (3)**, 507–528, https://doi.org/10.5194/esd-8-507-2017.

Kendon, E., A. Prein, C. Senior, and A. Stirling, 2021: Challenges and outlook for convection-permitting climate modelling. *Philosophical Transactions of the Royal Society A*, **379 (2195)**, 20190 547, https://doi.org/10.1098/rsta.2019.0547.

Kendon, E. J., N. M. Roberts, C. A. Senior, and M. J. Roberts, 2012: Realism of rainfall in a very high-resolution regional climate model. *Journal of Climate*, **25 (17)**, 5791–5806, https://doi.org/10.1175/JCLI-D-11-00562.1.

Kendon, E. J., R. A. Stratton, S. Tucker, J. H. Marsham, S. Berthou, D. P. Rowell, and C. A. Senior, 2019: Enhanced future changes in wet and dry extremes over africa at convection-permitting scale. *Nature communications*, **10 (1)**, 1–14, https://doi.org/10.1038/s41467-019-09776-9.

Kouadio, K., S. Bastin, A. Konare, and V. O. Ajayi, 2020: Does convection-permitting simulate better rainfall distribution and extreme over guinean coast and surroundings? *Climate Dynamics*, **55 (1)**, 153–174, https://doi.org/10.1007/s00382-018-4308-y.

Lavin-Gullon, A., M. Feijoó, S. Solman, J. Fernández, R. da Rocha, and M. L. Bettolli, 2021: Synoptic forcing associated with extreme precipitation events over southeastern south america as depicted by a cordex fps set of convection-permitting rcms. *Climate Dynamics*, **56**, 3187–3203, https://doi.org/10.1007/s00382-021-05637-8.

Lawrence, D. M., and Coauthors, 2011: Parameterization improvements and functional and structural advances in version 4 of the community land model. *Journal of Advances in Modeling Earth Systems*, **3 (1)**, https://doi.org/10.1029/2011MS00045.

Leung, L. R., L. O. Mearns, F. Giorgi, and R. L. Wilby, 2003: Regional climate research: Needs and opportunities. *Bulletin of the American Meteorological Society*, **84 (1)**, 89–95, https://doi.org/10.1175/BAMS-84-1-89.

Li, P., K. Furtado, T. Zhou, H. Chen, and J. Li, 2021: Convection-permitting modelling improves simulated precipitation over the central and eastern tibetan plateau. *Quarterly Journal of the Royal Meteorological Society*, **147 (734)**, 341–362, https://doi.org/10.1002/qj.3921.

Li, P., K. Furtado, T. Zhou, H. Chen, J. Li, Z. Guo, and C. Xiao, 2020: The diurnal cycle of east asian summer monsoon precipitation simulated by the met office unified model at convection-permitting scales. *Climate Dynamics*, **55 (1)**, 131–151, https://doi.org/10.1007/s00382-018-4368-z.

Lind, P., and Coauthors, 2020: Benefits and added value of convection-permitting climate modeling over fenno-scandinavia. *Climate Dynamics*, **55 (7)**, 1893–1912, https://doi.org/10.1007/s00382-020-05359-3.

Liu, C., and Coauthors, 2017: Continental-scale convection-permitting modeling of the current and future climate of north america. *Climate Dynamics*, **49 (1)**, 71–95, https://doi.org/10.1007/s00382-016-3327-9.

Lucas-Picher, P., D. Argüeso, E. Brisson, Y. Tramblay, P. Berg, A. Lemonsu, S. Kotlarski, and C. Caillaud, 2021: Convection-permitting modeling with regional climate models: Latest developments and next steps. *Wiley Interdisciplinary Reviews: Climate Change*, **12 (6)**, e731, https://doi.org/10.1002/wcc.731.

Lucas-Picher, P., R. Laprise, and K. Winger, 2017: Evidence of added value in north american regional climate model hindcast simulations using ever-increasing horizontal resolutions. *Climate Dynamics*, **48 (7-8)**, 2611–2633, https://doi.org/10.1007/s00382-016-3227-z.

Marengo, J. A., M. W. Douglas, and P. L. Silva Dias, 2002: The south american low-level jet east of the andes during the 1999 lba-trmm and lba-wet amc campaign. *Journal of Geophysical Research: Atmospheres*, **107 (D20)**, LBA–47, https://doi.org/10.1029/2001JD001188.

Marengo, J. A., and Coauthors, 2010: Future change of climate in south america in the late twenty-first century: intercomparison of scenarios from three regional climate models. *Climate Dynamics*, **35**, 1073–1097, https://doi.org/10.1007/s00382-009-0721-6.

Martinez, J. A., P. A. Arias, C. Castro, H.-I. Chang, and C. A. Ochoa-Moya, 2019: Sea surface temperature-related response of precipitation in northern south america according to a wrf multi-decadal simulation. *International Journal of Climatology*, **39 (4)**, 2136–2155, https://doi.org/10.1002/joc.5940.

Martinez, J. A., P. A. Arias, C. Junquas, J. C. Espinoza, T. Condom, F. Dominguez, and J. S. Morales, 2022: The orinoco low-level jet and the cross-equatorial moisture transport over tropical south america: Lessons from seasonal wrf simulations. *Journal of Geophysical Research: Atmospheres*, **127 (3)**, e2021JD035 603, https://doi.org/10.1029/2021JD035603.

Meroni, A. N., K. A. Oundo, R. Muita, M.-J. Bopape, T. R. Maisha, M. Lagasio, A. Parodi, and G. Venuti, 2021: Sensitivity of some african heavy rainfall events to microphysics and planetary boundary layer schemes: Impacts on localised storms. *Quarterly Journal of the Royal Meteorological Society*, **147 (737)**, 2448–2468, https://doi.org/10.1002/qj.4033.

Miguez-Macho, G., G. L. Stenchikov, and A. Robock, 2004: Spectral nudging to eliminate the effects of domain position and geometry in regional climate model simulations. *Journal of Geophysical Research: Atmospheres*, **109 (D13)**, https://doi.org/10.1029/2003JD004495.

Mohr, K. I., D. Slayback, and K. Yager, 2014: Characteristics of precipitation features and annual rainfall during the trmm era in the central andes. *Journal of climate*, **27 (11)**, 3982–4001, https://doi.org/10.1175/JCLI-D-13-00592.1.

Montini, T. L., C. Jones, and L. M. Carvalho, 2019: The south american low-level jet: A new climatology, variability, and changes. *Journal of Geophysical Research: Atmospheres*, **124 (3)**, 1200–1218, https://doi.org/10.1029/2018JD029634.

Morrison, H., G. Thompson, and V. Tatarskii, 2009: Impact of cloud microphysics on the development of trailing stratiform precipitation in a simulated squall line: Comparison of one-and two-moment schemes. *Monthly weather review*, **137 (3)**, 991–1007, https://doi.org/10.1175/2008MWR2556.1.

Moufouma-Okia, W., and R. Jones, 2015: Resolution dependence in simulating the african hydroclimate with the hadgem3-ra regional climate model. *Climate Dynamics*, **44 (3-4)**, 609–632, https://doi.org/10.1007/s00382-014-2322-2.

Mourre, L., T. Condom, C. Junquas, T. Lebel, J. E Sicart, R. Figueroa, and A. Cochachin, 2016: Spatio-temporal assessment of wrf, trmm and in situ precipitation data in a tropical mountain environment (cordillera blanca, peru). *Hydrology and Earth System Sciences*, **20 (1)**, 125–141, https://doi.org/10.5194/hess-20-125-2016.

Moya-Álvarez, A. S., D. Martínez-Castro, S. Kumar, R. Estevan, and Y. Silva, 2019: Response of the wrf model to different resolutions in the rainfall forecast over the complex peruvian orography. *Theoretical and Applied Climatology*, **137**, 2993–3007, https://doi.org/10.1007/s00704-019-02782-3.

Nakanishi, M., and H. Niino, 2009: Development of an improved turbulence closure model for the atmospheric boundary layer. *Journal of the Meteorological Society of Japan. Ser. II*, **87 (5)**, 895–912, https://doi.org/10.2151/jmsj.87.895.

Nicolini, M., and Y. G. Skabar, 2011: Diurnal cycle in convergence patterns in the boundary layer east of the andes and convection. *Atmospheric Research*, **100 (4)**, 377–390, https://doi.org/10.1016/j.atmosres.2010.09.019.

Niu, G.-Y., and Coauthors, 2011: The community noah land surface model with multiparameterization options (noah-mp): 1. model description and evaluation with local-scale measurements. *Journal of Geophysical Research: Atmospheres*, **116 (D12)**, https://doi.org/10.1029/2010JD015139.

Paccini, L., and B. Stevens, 2023: Assessing precipitation over the amazon basin as simulated by a storm-resolving model. *Journal of Geophysical Research: Atmospheres*, **128 (4)**, e2022JD037 436, https://doi.org/10.1029/2022JD037436.

Pleim, J. E., 2007: A combined local and nonlocal closure model for the atmospheric boundary layer. part i: Model description and testing. *Journal of Applied Meteorology and Climatology*, **46 (9)**, 1383–1395, https://doi.org/10.1175/JAM2539.1.

Poveda, G., J. C. Espinoza, M. D. Zuluaga, S. A. Solman, R. Garreaud, and P. J. Van Oevelen, 2020: High impact weather events in the andes. *Frontiers in Earth Science*, **8**, 162, https://doi.org/10.3389/feart.2020.00162.

Prein, A., A. Gobiet, M. Suklitsch, H. Truhetz, N. Awan, K. Keuler, and G. Georgievski, 2013: Added value of convection permitting seasonal simulations. *Climate Dynamics*, **41 (9-10)**, 2655–2677, https://doi.org/10.1007/s00382-013-1744-6.

Prein, A. F., M. Ge, A. R. Valle, D. Wang, and S. E. Giangrande, 2022: Towards a unified setup to simulate mid-latitude and tropical mesoscale convective systems at kilometer-scales. *Earth and Space Science*, **9 (8)**, e2022EA002 295, https://doi.org/10.1029/2022EA002295.

Prein, A. F., C. Liu, K. Ikeda, R. Bullock, R. M. Rasmussen, G. J. Holland, and M. Clark, 2020: Simulating north american mesoscale convective systems with a convection-permitting climate model. *Climate Dynamics*, **55 (1)**, 95–110, https://doi.org/10.1007/s00382-017-3993-2.

Prein, A. F., and Coauthors, 2015: A review on regional convection-permitting climate modeling: Demonstrations, prospects, and challenges. *Reviews of geophysics*, **53 (2)**, 323–361, https://doi.org/10.1002/2014RG000475.

Rasmussen, K., and R. Houze Jr, 2016: Convective initiation near the andes in subtropical south america. *Monthly Weather Review*, **144 (6)**, 2351–2374, https://doi.org/10.1175/MWR-D-15-0058.1.

Roads, J., and Coauthors, 2003: International research institute/applied research centers (iri/arcs) regional model intercomparison over south america. *Journal of Geophysical Research: Atmospheres*, **108 (D14)**, https://doi.org/10.1029/2002JD003201.

Romatschke, U., and R. A. Houze Jr, 2010: Extreme summer convection in south america. *Journal of Climate*, **23 (14)**, 3761–3791, https://doi.org/10.1175/2010JCLI3465.1.

Rummukainen, M., 2016: Added value in regional climate modeling. *Wiley Interdisciplinary Reviews: Climate Change*, **7 (1)**, 145–159, https://doi.org/10.1002/wcc.378.

Rummukainen, M., B. Rockel, L. Bärring, J. H. Christensen, and M. Reckermann, 2015: Twenty-first-century challenges in regional climate modeling. *Bulletin of the American Meteorological Society*, **96 (8)**, ES135–ES138, https://doi.org/10.1175/BAMS-D-14-00214.1.

Salio, P., M. Nicolini, and E. J. Zipser, 2007: Mesoscale convective systems over southeastern south america and their relationship with the south american low-level jet. *Monthly Weather Review*, **135 (4)**, 1290–1309, https://doi.org/10.1175/MWR3305.1.

Saulo, A., M. Nicolini, and S. C. Chou, 2000: Model characterization of the south american low-level flow during the 1997–1998 spring–summer season. *Climate Dynamics*, **16 (10)**, 867–881, https://doi.org/10.1007/s003820000085.

Schumacher, V., A. Fernández, F. Justino, and A. Comin, 2020: Wrf high resolution dynamical downscaling of precipitation for the central andes of chile and argentina. *Frontiers in Earth Science*, **8**, 328, https://doi.org/10.3389/feart.2020.00328.

Skamarock, W. C., and Coauthors, 2019: A description of the advanced research wrf model version 4. *National Center for Atmospheric Research: Boulder, CO, USA*, 145, https://doi.org/10.5065/1dfh-6p97.

Solman, S. A., 2013: Regional climate modeling over south america: a review. *Advances in Meteorology*, **2013**, 1–13, https://doi.org/10.1155/2013/504357.

Solman, S. A., and J. Blázquez, 2019: Multiscale precipitation variability over south america: analysis of the added value of cordex rcm simulations. *Climate Dynamics*, **53 (3-4)**, 1547–1565, https://doi.org/10.1007/s00382-019-04689-1.

Stratton, R. A., and Coauthors, 2018: A pan-african convection-permitting regional climate simulation with the met office unified model: Cp4-africa. *Journal of Climate*, **31 (9)**, 3485–3508, https://doi.org/10.1175/JCLI-D-17-0503.1.

Sun, X., M. Xue, J. Brotzge, R. A. McPherson, X.-M. Hu, and X.-Q. Yang, 2016: An evaluation of dynamical downscaling of central plains summer precipitation using a wrf-based regional climate model at a convection-permitting 4 km resolution. *Journal of Geophysical Research: Atmospheres*, **121 (23)**, 13–801, https://doi.org/10.1002/2016JD024796.

Sungmin, O., and P.-E. Kirstetter, 2018: Evaluation of diurnal variation of gpm imerg-derived summer precipitation over the contiguous us using mrms data. *Quarterly Journal of the Royal Meteorological Society*, **144**, 270–281, https://doi.org/10.1002/qj.3218.

Tan, J., G. J. Huffman, D. T. Bolvin, and E. J. Nelkin, 2019: Diurnal cycle of imerg v06 precipitation. *Geophysical Research Letters*, **46 (22)**, 13 584–13 592, https://doi.org/10.1029/2019GL085395.

Taraphdar, S., and Coauthors, 2021: Wrf gray-zone simulations of precipitation over the middle-east and the uae: Impacts of physical parameterizations and resolution. *Journal of Geophysical Research: Atmospheres*, **126 (10)**, e2021JD034 648, https://doi.org/10.1029/2021JD034648.

Taylor, K. E., 2001: Summarizing multiple aspects of model performance in a single diagram. *Journal of Geophysical Research: Atmospheres*, **106 (D7)**, 7183–7192, https://doi.org/10.1029/2000JD900719.

Thompson, G., and T. Eidhammer, 2014: A study of aerosol impacts on clouds and precipitation development in a large winter cyclone. *Journal of the atmospheric sciences*, **71 (10)**, 3636–3658, https://doi.org/10.1175/JAS-D-13-0305.1.

Thompson, G., P. R. Field, R. M. Rasmussen, and W. D. Hall, 2008: Explicit forecasts of winter precipitation using an improved bulk microphysics scheme. part ii: Implementation of a new snow parameterization. *Monthly Weather Review*, **136 (12)**, 5095–5115, https://doi.org/10.1175/2008MWR2387.1.

Tiedtke, M., 1989: A comprehensive mass flux scheme for cumulus parameterization in large-scale models. *Monthly weather review*, **117 (8)**, 1779–1800, https://doi.org/10.1175/1520-0493(1989)117⟨1779:ACMFSF⟩2.0.CO;2.

Torma, C., F. Giorgi, and E. Coppola, 2015: Added value of regional climate modeling over areas characterized by complex terrain—precipitation over the alps. *Journal of Geophysical Research: Atmospheres*, **120 (9)**, 3957–3972, https://doi.org/10.1002/2014JD022781.

Trier, S., C. Davis, and D. Ahijevych, 2010: Environmental controls on the simulated diurnal cycle of warm-season precipitation in the continental united states. *Journal of the atmospheric sciences*, **67 (4)**, 1066–1090, https://doi.org/10.1175/2009JAS3247.1.

977 Vera, C., and Coauthors, 2006: The south american low-level jet experiment. *Bulletin of the*
978 *American Meteorological Society*, **87 (1)**, 63–78, https://doi.org/10.1175/BAMS-87-1-63.

979 Vernekar, A. D., B. P. Kirtman, and M. J. Fennessy, 2003: Low-level jets and their effects on the
980 south american summer climate as simulated by the ncep eta model. *Journal of Climate*, **16 (2)**,
981 297–311, https://doi.org/10.1175/1520-0442(2003)016⟨0297:LLJATE⟩2.0.CO;2.

982 Watters, D., and A. Battaglia, 2019: The summertime diurnal cycle of precipitation derived from
983 imerg. *Remote Sensing*, **11 (15)**, 1781, https://doi.org/10.3390/rs11151781.

984 Xue, M., X. Luo, K. Zhu, Z. Sun, and J. Fei, 2018: The controlling role of boundary layer inertial
985 oscillations in meiyu frontal precipitation and its diurnal cycles over china. *Journal of Geophys-*
986 *ical Research: Atmospheres*, **123 (10)**, 5090–5115, https://doi.org/10.1029/2018JD028368.

987 Yun, Y., C. Liu, Y. Luo, X. Liang, L. Huang, F. Chen, and R. Rasmmusen, 2020: Convection-
988 permitting regional climate simulation of warm-season precipitation over eastern china. *Climate*
989 *Dynamics*, **54 (3)**, 1469–1489, https://doi.org/10.1007/s00382-019-05070-y.

990 Zaninelli, P. G., C. G. Menéndez, M. Falco, N. López-Franca, and A. F. Carril, 2019: Future
991 hydroclimatological changes in south america based on an ensemble of regional climate models.
992 *Climate Dynamics*, **52**, 819–830, https://doi.org/10.1007/s00382-018-4225-0.

993 Zhang, Y., M. Xue, K. Zhu, and B. Zhou, 2019: What is the main cause of diurnal variation
994 and nocturnal peak of summer precipitation in sichuan basin, china? the key role of boundary
995 layer low-level jet inertial oscillations. *Journal of Geophysical Research: Atmospheres*, **124 (5)**,
996 2643–2664, https://doi.org/10.1029/2018JD029834.

997 Zhu, K., and M. Xue, 2016: Evaluation of wrf-based convection-permitting multi-physics ensemble
998 forecasts over china for an extreme rainfall event on 21 july 2012 in beijing. *Advances in*
999 *Atmospheric Sciences*, **33 (11)**, 1240–1258, https://doi.org/10.1007/s00376-016-6202-z.

1000 Zhu, K., and Coauthors, 2018: Evaluation of real-time convection-permitting precipitation fore-
1001 casts in china during the 2013–2014 summer season. *Journal of Geophysical Research: Atmo-*
1002 *spheres*, **123 (2)**, 1037–1064, https://doi.org/10.1002/2017JD027445.